

Banner appropriate to article type will appear here in typeset article

# Large-scale streaks in a turbulent bluff body wake

Akhil Nekkanti<sup>1</sup>†, Sheel Nidhan<sup>1</sup>, Oliver T. Schmidt<sup>1</sup> and Sutanu Sarkar<sup>1</sup>‡

<sup>1</sup>Department of Mechanical and Aerospace Engineering, University of California San Diego, CA 92093, USA

(Received 17 April 2023; revised 28 July 2023; accepted 9 September 2023)

A turbulent circular disk wake database (Chongsiripinyo & Sarkar, *J. Fluid Mech.*, vol. 885, 2020) at Reynolds number  $Re = U_\infty D/\nu = 5 \times 10^4$  is interrogated to identify the presence of large-scale streaks - coherent elongated regions of streamwise velocity. The unprecedented streamwise length - until  $x/D \approx 120$  - of the simulation enables investigation of the near and far wake. The near wake is dominated by the vortex shedding (VS) mode residing at azimuthal wavenumber  $m = 1$  and Strouhal number  $St = 0.135$ . After filtering out the VS structure, conclusive evidence of large-scale streaks with frequency  $St \rightarrow 0$ , equivalently streamwise wavenumber  $k_x \rightarrow 0$  in the wake, becomes apparent in visualizations and spectra. These streaky structures are found throughout the simulation domain beyond  $x/D \approx 10$ . Conditionally averaged streamwise vorticity fields reveal that the lift-up mechanism is active in the near as well as the far wake, and that ejections contribute more than sweeps to events of intense  $-u'_x u'_r$ . Spectral proper orthogonal decomposition (SPOD) is employed to extract the energy and the spatiotemporal features of the large-scale streaks. The streak energy is concentrated in the  $m = 2$  azimuthal mode over the entire domain. Finally, bispectral mode decomposition (BMD) is conducted to reveal strong interaction between  $m = 1$  and  $St = \pm 0.135$  modes to give the  $m = 2, St \rightarrow 0$  streak mode. Our results indicate that the self-interaction of the VS mode generates the  $m = 2, St \rightarrow 0$  streamwise vortices, which leads to streak formation through the lift-up process. To the authors' knowledge, this is the first study that reports and characterizes large-scale low-frequency streaks and the associated lift-up mechanism in a turbulent wake.

**Key words:**

## 1. Introduction

Coherent structures, which are organized patterns of motion in a seemingly random turbulent flow field, play an essential role in turbulent shear flows. Among these structures, streaks are among the most widely discussed, particularly in wall-bounded flows, where they were identified experimentally (Kline *et al.* 1967) as elongated regions of streamwise velocity in the near-wall region. As these streaks break up, they transfer energy from the inner to the

† Present address: Division of Engineering and Applied Science, California Institute of Technology, Pasadena, CA 91125, USA

‡ Email address for correspondence: sarkar@ucsd.edu

outer layers, thereby maintaining turbulence in the outer layers of the boundary layer (Kim *et al.* 1971). This process, also known as *bursting*, can account for up to 75% of Reynolds stresses (Lu & Willmarth 1973), hence assisting in the production of turbulent kinetic energy (TKE). Smith & Metzler (1983) found that low-speed streaks are robust features of boundary layers, occurring across a wide range of Reynolds numbers ( $740 < Re_\theta < 5830$ ). Their spanwise spacing of 100 wall units was found to be invariant with  $Re_\theta$ . Hutchins & Marusic (2007) investigated the logarithmic region of the boundary layer, finding that the streaks in this region are distinct and much larger than the near-wall streaks, extending up to 20 times the boundary layer thickness. Building upon this work, Monty *et al.* (2007) reported the existence of streaks in the logarithmic region of turbulent pipe and channel flows as well. They also found that the width of these structures in channel and pipe flows is larger than those of the boundary layer.

The presence of a wall is not a prerequisite for the formation of streaks (Jiménez & Pinelli 1999; Mizuno & Jiménez 2013). A few studies in the past (see figure 8b Brown & Roshko 1974; Bernal & Roshko 1986; Liepmann & Gharib 1992) have reported the presence of streak-like structures in the mixing layer, with the latter two showing increasing amplification of the streaks as the flow progresses downstream. More attention has been paid to the role of streaks in the mixing layer and specially the jet, recently. Jiménez-González & Brancher (2017) performed transient growth analysis in round jets finding that, for optimal initial disturbances, the streamwise vortices evolve to produce streamwise streaks. Marant & Cossu (2018) also reported similar findings in a hyperbolic-tangent mixing layer. Nogueira *et al.* (2019) applied spectral proper orthogonal decomposition on a PIV dataset of a circular turbulent jet at a high Reynolds number and demonstrated the presence of large-scale streaky structures in the near field (until  $x/D = 8$ ). They further demonstrated that these structures exhibit large time scales and are associated with a low frequency of  $St \rightarrow 0$ . The numerical counterpart of the previous study was performed by Pickering *et al.* (2020). They found that the streaky structures near the nozzle exit are dominated by higher azimuthal wavenumbers and the dominance shifts to lower azimuthal wavenumbers downstream, with  $m = 2$  dominating by  $x/D = 30$ . A similar conclusion about the dominance of  $m = 2$  was reached by Samie *et al.* (2022) who utilized quadrant analysis on a low Reynolds number jet.

In wall-bounded flows, streaks are generated by the lift-up mechanism (Ellingsen & Palm 1975; Landahl 1975). Streamwise vortices induce wall-normal velocities, bringing fluid from high-speed to low-speed regions and vice-versa to form streaks, hence the term ‘lift-up’. The subsequent instability and breakdown of these streaks are important to the self-sustaining cycle of wall turbulence (Hamilton *et al.* 1995; Waleffe 1997). Brandt (2014) presents a detailed review of the theory behind the lift-up mechanism and its role in transitional and turbulent flows. Although originally introduced as an instability mechanism that destabilizes a streamwise-independent base flow, the lift-up mechanism has been found to be dynamically crucial to fully turbulent wall-bounded flows as well (Jiménez 2018; Bae *et al.* 2021; Farrell & Ioannou 2012).

The lift-up mechanism is active and plays a critical role in jets too. In their resolvent analysis of data from a turbulent jet experiment, Nogueira *et al.* (2019) found that the optimal forcing modes at  $St \rightarrow 0$  take the form of streamwise vortices that eject high-speed fluid and sweep low-speed fluid, depending on the orientation of these vortices. Pickering *et al.* (2020) analyzed a turbulent jet LES database, finding that the response modes of these lift-up dominated optimal forcing modes indeed take the form of streamwise streaks. While these studies focused on circular jets, Lasagna *et al.* (2021) found that the lift-up mechanism is active in the near field of fractal jets as well.

As discussed in the foregoing, there has been a growing interest in the investigation of streaky structures and lift-up mechanisms in free shear flows, particularly in turbulent jets.

These experimental and numerical studies have confirmed that the presence of a wall is not necessary for the formation of streaks, which has motivated us to explore another important class of free shear flows, i.e., turbulent wakes. Previous wake studies have primarily focused on the vortex shedding mechanism. Near the body and in the intermediate wake, the vortex shedding (VS) mode emerges as the most dominant coherent structure (Taneda 1978; Cannon *et al.* 1993; Berger *et al.* 1990; Yun *et al.* 2006). However, it is worth noting that Johansson *et al.* (2002) reported the presence of a distinct very low-frequency mode,  $St \rightarrow 0$ , at azimuthal wavenumber  $m = 2$  in their proper orthogonal decomposition (POD) analyses of the turbulent wake of a circular disk at  $Re \approx 2.5 \times 10^4$ . This mode is distinct from the VS mode of a circular disk wake, which resides at  $m = 1$  with  $St = 0.135$  (Berger *et al.* 1990). In a subsequent study, Johansson & George (2006) extended the downstream distance to  $x/D = 150$  and found that the  $m = 2$  mode with  $St \rightarrow 0$  dominated the far wake of the disk in terms of energy content relative to the vortex shedding mode. This finding was corroborated in the spectral POD analysis (Nidhan *et al.* 2020) of a disk wake at a higher Reynolds number ( $Re = 5 \times 10^4$ ). The authors further found low-rank behavior of the SPOD modes and that almost the entire Reynolds shear stress could be reconstructed with the leading SPOD modes of  $m \leq 4$ . Streamwise-elongated streaks, a focus of the current paper, were not considered by Nidhan *et al.* (2020).

None of the wake studies that report the presence and the eventual dominance at large  $x$  of the very low-frequency mode ( $St \rightarrow 0$ ) at  $m = 2$  explain the physical origins of this structure. To address this gap, we revisit the LES database of Chongsiripinyo & Sarkar (2020), who simulated the wake of a circular disk up to an unprecedented downstream distance of  $x/D = 125$ . The large streamwise domain enables us to investigate the entire wake. Unlike the previous SPOD analysis (Nidhan *et al.* 2020) of this wake database, we focus on the streaky structures. We attempt to answer the following questions: Can streaky structures be identified in the near and far field of the turbulent wake? Is the lift-up mechanism active in the turbulent wake? How do the energetics and spatial structure of streaks evolve with downstream distance? What, if any, is the link between the streak and the well-documented and extensively studied vortex shedding mode?

In this work, besides visualizations and classical statistical analyses, we utilize two modal techniques, spectral proper orthogonal decomposition (SPOD) and bispectral mode decomposition (BMD), to shed light on the aforementioned questions. SPOD, whose mathematical framework in the context of turbulent flow was laid out by Lumley (1967, 1970), extracts a set of orthogonal modes sorted according to their energy at each frequency. It distinguishes the different time scales of the flow and identifies the most energetic coherent structures at each time scale. SPOD modes are coherent in both space and time and represent the flow structures in a statistical sense (Towne *et al.* 2018). Early applications of SPOD were by Glauser *et al.* (1987); Glauser & George (1992); Delville (1994) and this method has regained popularity since the work by Towne *et al.* (2018); Schmidt *et al.* (2018). SPOD is particularly suitable for detecting and educing modes corresponding to streaky structures in statistically stationary flows (Nogueira *et al.* 2019; Pickering *et al.* 2020; Abreu *et al.* 2020), and is hence employed in this work. Bispectral mode decomposition, proposed by Schmidt (2020), extracts the flow structures that are generated through triadic interactions. It identifies the most dominant triads in the flow by maximizing the spatially-integrated bispectrum. Furthermore, it picks out the spatial regions of nonlinear interactions between the coherent structures. BMD has been used to characterize the triadic interactions in various flow configurations, such as laminar-turbulent transition on a flat plate (Goparaju & Gaitonde 2022), forced jets (Maia *et al.* 2021; Nekkanti *et al.* 2022, 2023), swirling flows (Moczarski *et al.* 2022) and wake of an airfoil (Patel & Yeh 2023). In this work, we will employ BMD

to investigate the presence and strength of nonlinear interactions between the VS mode and the streak-containing modes.

The manuscript is organized as follows. In §2, the dataset and numerical methodology of SPOD and BMD are discussed. §3 presents the extraction and visualization of streaks and lift-up mechanism in the near and far wake. Results from SPOD analysis at different downstream locations are presented in §4 with a particular emphasis again on streaks and lift-up mechanism. §5 presents the results from the analysis of nonlinear interactions in the wake at select locations. The manuscript ends with discussion and conclusions in §6.

## 2. Numerical wake database and methods for its analysis

### 2.1. Dataset description

The dataset employed for the present study of wake dynamics is from the high-resolution large eddy simulation (LES) of flow past a circular disk at Reynolds number,  $Re = U_\infty D / \nu = 5 \times 10^4$ , reported in Chongsiripinyo & Sarkar (2020). Here  $U_\infty$  is the freestream velocity,  $D$  is the disk diameter, and  $\nu$  is the kinematic viscosity. The case of a homogeneous fluid from Chongsiripinyo & Sarkar (2020), who also simulate stratified wakes, is selected here. The filtered Navier-Stokes equations, subject to the condition of solenoidal velocity, were numerically solved on a structured cylindrical grid that spans a radial distance of  $r/D = 15$  and a streamwise distance of  $x/D = 125$ . An immersed boundary method (Balaras 2004) is used to represent the circular disk in the simulation domain and the dynamic Smagorinsky model (Germano *et al.* 1991) is used for the LES model. The number of grid points in the radial ( $r$ ), azimuthal ( $\theta$ ) and streamwise directions ( $x$ ) are  $N_r = 365$ ,  $N_\theta = 256$  and  $N_x = 4096$ , respectively. The simulation has high resolution with streamwise grid resolution of  $\Delta x = 10\eta$  at  $x/D = 10$ , where  $\eta$  is the Kolmogorov lengthscale. By  $x/D = 125$ , the resolution improves to  $\Delta x < 6\eta$  so that the onus on the subgrid model progressively decreases. Readers are referred to Chongsiripinyo & Sarkar (2020) for a detailed description of the numerical methodology and grid quality.

### 2.2. Spectral proper orthogonal decomposition (SPOD)

SPOD is the frequency-domain variant of proper orthogonal decomposition. It computes monochromatic modes that are optimal in terms of the energy norm of the flow, e.g., turbulent kinetic energy (TKE) for the wake flow at hand. The SPOD modes are the eigenvectors of the cross-spectral density matrix, which is estimated using Welch's approach (Welch 1967). Here, we provide a brief overview of the method. For a detailed mathematical derivation and algorithmic implementation, readers are referred to Towne *et al.* (2018) and Schmidt & Colonius (2020).

For a statistically stationary flow, let  $\mathbf{q}_i = \mathbf{q}(t_i)$  denote the mean subtracted snapshots, where  $i = 1, 2, \dots, n_t$  are  $n_t$  number of snapshots. For spectral estimation, the dataset is first segment into  $n_{\text{blk}}$  overlapping blocks with  $n_{\text{fft}}$  snapshots in each block. The neighbouring blocks overlap by  $n_{\text{ovlp}}$  snapshots with  $n_{\text{ovlp}} = n_{\text{fft}}/2$ . The  $n_{\text{blk}}$  blocks are then Fourier transformed in time and all Fourier realizations of the  $l$ -th frequency,  $\mathbf{q}_l^{(j)}$ , are arranged in a matrix,

$$\hat{\mathbf{Q}}_l = \left[ \hat{\mathbf{q}}_l^{(1)}, \hat{\mathbf{q}}_l^{(2)}, \dots, \hat{\mathbf{q}}_l^{(n_{\text{blk}})} \right]. \quad (2.1)$$

The SPOD eigenvalues,  $\Lambda_l$ , are obtained by solving the following eigenvalue problem:

$$\frac{1}{n_{\text{blk}}} \hat{\mathbf{Q}}_l^* \mathbf{W} \hat{\mathbf{Q}}_l \Psi_l = \Psi_l \Lambda_l, \quad (2.2)$$

where  $\mathbf{W}$  is a positive-definite Hermitian matrix that accounts for the component-wise and numerical quadrature weights and  $(\cdot)^*$  denotes the complex conjugate. SPOD modes at the  $l$ -th frequency are recovered as

$$\Phi_l = \frac{1}{\sqrt{n_{\text{blk}}}} \hat{\mathbf{Q}}_l \Psi_l \Lambda_l^{-1/2}. \quad (2.3)$$

The SPOD eigenvalues are denoted by  $\Lambda_l = \text{diag}(\lambda_l^{(1)}, \lambda_l^{(2)}, \dots, \lambda_l^{(n_{\text{blk}})})$ . By construction,  $\lambda_l^{(1)} \geq \lambda_l^{(2)} \geq \dots \geq \lambda_l^{(n_{\text{blk}})}$  represent the energies of the corresponding SPOD modes that are given by the column vectors of the matrix  $\Phi_l = [\phi_l^{(1)}, \phi_l^{(2)}, \dots, \phi_l^{(n_{\text{blk}})}]$ . The SPOD mode  $\phi_l^{(j)}$  represents the  $j$ -th dominant coherent flow structure at the  $l$ -th frequency. An useful property of the SPOD modes is their orthogonality; the weighted inner product at each frequency,  $\langle \phi_l^{(i)}, \phi_l^{(j)} \rangle = (\phi_l^{(i)})^* \mathbf{W} \phi_l^{(j)} = \delta_{ij}$ .

Here, we perform SPOD on various 2D streamwise planes ranging from  $x/D = 1$  to 120. Thus,  $\mathbf{q}$  contains the three velocity components at the discretized grid nodes on a streamwise-constant plane. These planes are sampled at a spacing of  $5D$  from  $x/D = 5$  to  $x/D = 100$ , and five additional planes are sampled at  $x/D = 1, 2, 3, 110$ , and 120. The utilized time series has  $n_t = 7200$  snapshots with a uniform separation of non-dimensional time of  $\Delta t U_\infty / D = 0.072$  between two snapshots. Owing to the periodicity in the azimuthal direction, the flow field is first decomposed into azimuthal wavenumbers  $m$ ,

$$q(x, r, \theta, t) = \sum_m \hat{q}_m(x, r, t), \quad (2.4)$$

and then SPOD is applied on the data at each azimuthal wavenumber. The spectral estimation parameters used here are  $n_{\text{fft}} = 512$  and  $n_{\text{ovlp}} = 256$ , resulting in  $n_{\text{blk}} = 27$  SPOD modes for each  $St$ . Each block used for the temporal FFT spans a time duration of  $\Delta T = 36.91 U_\infty / D$ .

### 2.3. Reconstruction using convolution approach

The convolution strategy proposed by Nekkanti & Schmidt (2021) is employed for low-dimensional reconstruction of the flow field. This involves computing the expansion coefficients by convolving the SPOD modes over the data one snapshot at a time,

$$\mathbf{a}_l^{(i)}(t) = \int_{\Delta T} \int_{\Omega} (\phi_l^{(i)}(x))^* \mathbf{W}(x) \mathbf{q}(x, t + \tau) w(\tau) e^{-i2\pi f_l \tau} dx d\tau. \quad (2.5)$$

Here,  $w(\tau)$  is the Hamming windowing function and  $\Omega$  is the spatial domain of interest. The data at time  $t$  is then reconstructed as

$$\mathbf{q}(t) \approx \sum_l \sum_i a_l^{(i)}(t) \phi_l^{(i)} e^{-i2\pi f_l t}. \quad (2.6)$$

### 2.4. Bispectral mode decomposition

Bispectral mode decomposition (BMD) is a technique recently proposed by Schmidt (2020), to characterize the coherent structures associated with triadic interactions in statistically stationary flows. Here, we provide a brief overview of the method. The reader is referred to Schmidt (2020) for further details of the derivation and mathematical properties of the method.

BMD is an extension of classical bispectral analysis to multidimensional data. The classical bispectrum is defined as the double Fourier transform of the third moment of a time signal. For a time series,  $y(t)$  with zero mean, the bispectrum is

$$S_{yyy}(f_1, f_2) = \int \int R_{yyy}(\tau_1, \tau_2) e^{-i2\pi(f_1\tau_1 + f_2\tau_2)} d\tau_1 d\tau_2, \quad (2.7)$$

where  $R_{yyy}(\tau_1, \tau_2) = E[y(t)y(t - \tau_1)y(t - \tau_2)]$  is the third moment of  $y(t)$ , and  $E[\cdot]$  is the expectation operator. The bispectrum is a signal processing tool for one-dimensional time series which only measures the quadratic phase coupling at a single spatial point. In contrast, BMD identifies the intensity of the triadic interactions over the spatial domain of interest and extracts the corresponding spatially coherent structures.

BMD maximizes the spatial integral of the point-wise bispectrum,

$$b(f_k, f_l) = E \left[ \int_{\Omega} \hat{\mathbf{q}}^*(x, f_k) \circ \hat{\mathbf{q}}^*(x, f_l) \circ \hat{\mathbf{q}}(x, f_k + f_l) dx \right]. \quad (2.8)$$

Here,  $\hat{\mathbf{q}}$  is the temporal Fourier transform of  $\mathbf{q}$  computed using the Welch approach (Welch 1967) and  $\circ$  denotes the Hadamard (or element-wise) product.

Next, as in equation (2.1), all the Fourier realizations at  $l$ -th frequency are arranged into the matrix,  $\hat{\mathbf{Q}}_l$ . The auto-bispectral matrix is then computed as

$$\mathbf{B} = \frac{1}{n_{\text{blk}}} \hat{\mathbf{Q}}_{k \circ l}^H \mathbf{W} \hat{\mathbf{Q}}_{k+l}, \quad (2.9)$$

where,  $\hat{\mathbf{Q}}_{k \circ l}^H = \hat{\mathbf{Q}}_k^* \circ \hat{\mathbf{Q}}_l^*$ .

To measure the interactions between different quantities, we construct the cross-bispectral matrix

$$\mathbf{B}_c = \frac{1}{n_{\text{blk}}} \left( \hat{\mathbf{Q}}_k^* \circ \hat{\mathbf{R}}_l^* \right) \mathbf{W} \hat{\mathbf{S}}_{k+l}. \quad (2.10)$$

In the present application, matrices  $\mathbf{Q}$ ,  $\mathbf{R}$ , and  $\mathbf{S}$  comprise the time series of the field variables at the azimuthal wavenumber triad,  $[m_1, m_2, m_3]$ .

Owing to the non-Hermitian nature of the bispectral matrix, the optimal expansion coefficients,  $\mathbf{a}_1$  are obtained by maximising the absolute value of the Rayleigh quotient of  $\mathbf{B}$  (or  $\mathbf{B}_c$ )

$$\mathbf{a}_1 = \arg \max_{\|\mathbf{a}\|=1} \left| \frac{\mathbf{a}^* \mathbf{B} \mathbf{a}}{\mathbf{a}^* \mathbf{a}} \right|. \quad (2.11)$$

The complex mode bispectrum is then obtained as

$$\lambda_1(f_k, f_l) = \left| \frac{\mathbf{a}_1^* \mathbf{B} \mathbf{a}_1}{\mathbf{a}_1^* \mathbf{a}_1} \right|. \quad (2.12)$$

Finally, the leading-order bispectral modes and the cross-frequency fields are recovered as

$$\phi_{k+l}^{(1)} = \hat{\mathbf{Q}}_{k+l} \mathbf{a}_1, \quad \text{and} \quad (2.13)$$

$$\phi_{k \circ l}^{(1)} = \hat{\mathbf{Q}}_{k \circ l} \mathbf{a}_1, \quad (2.14)$$

respectively. By construction, the bispectral modes and cross-frequency fields have the same set of expansion coefficients. This explicitly ensures the causal relation between the resonant frequency triad,  $(f_k, f_l, f_k + f_l)$ , where  $\hat{\mathbf{Q}}_{k \circ l}$  is the cause and  $\hat{\mathbf{Q}}_{k+l}$  is the effect. The complex mode bispectrum,  $\lambda_1$ , measures the intensity of the triadic interaction and the bispectral mode,  $\phi_{k+l}^{(1)}$ , represents the structures that results from the nonlinear triadic interaction.

Similar to SPOD, we perform BMD on various 2D streamwise planes and use the same

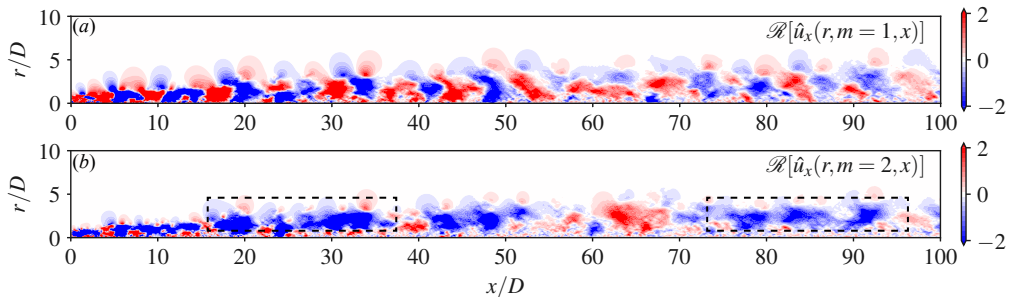


Figure 1: Azimuthally decomposed instantaneous fields of the streamwise velocity ( $u_x$ ) for (a)  $m = 1$  and (b)  $m = 2$  azimuthal modes. Rectangular boxes in (b) show large-scale streaks in the  $m = 2$  field.

spectral estimation parameters of  $n_{\text{fft}} = 512$  and  $n_{\text{ovlp}} = 256$ . Since our focus is on interactions of different azimuthal wavenumbers, the cross-BMD method, which computes the cross-bispectral matrix  $\mathbf{B}_c$ , is applied to the wake database. The specific interactions among different  $m$  and their analysis using BMD will be presented and discussed in §5.1.

### 3. Flow structures

#### 3.1. Streaky structures in the near and far wake

Nidhan *et al.* (2020) showed that the near and far field of the wake of a circular disk is dominated by two distinct modes residing at (a)  $m = 1, St = 0.135$  and (b)  $m = 2, St \rightarrow 0$ . While the former mode is the vortex shedding mode in the wake of a circular disk (Berger *et al.* 1990; Fuchs *et al.* 1979a; Cannon *et al.* 1993), the physical origin of the latter mode remains unclear. Johansson & George (2006) hint that the  $m = 2$  mode is linked to ‘very’ large-scale features that twist the mean flow slowly. Motivated by the findings of Nidhan *et al.* (2020) and the discussion in Johansson & George (2006), we investigate the streamwise manifestation of the azimuthal modes  $m = 1$  and  $m = 2$ . The main result is that, different from the  $m = 1$  mode, the  $m = 2$  mode is associated with streamwise-aligned streaky structures.

Figure 1 shows the azimuthal modes  $m = 1$  and  $m = 2$  of an instantaneous flow snapshot in the wake spanning downstream distance  $0 < x/D < 100$ , obtained using a Fourier transform in the azimuthal direction  $\theta$ . In the  $m = 1$  mode (figure 1a), a wavelength of  $\lambda/D = 1/St_{\text{VS}}$  (where the vortex shedding frequency,  $St_{\text{VS}} \approx 0.13 - 0.14$ ) is evident throughout the domain. This observation is in agreement with previous studies (Johansson *et al.* 2002; Johansson & George 2006; Nidhan *et al.* 2020) that report the existence of the vortex shedding mode at significantly large downstream locations  $\sim O(100D)$  from the disk.

The spatial structure of the  $m = 2$  mode (figure 1b) is quite different from that of the  $m = 1$  mode. In the  $m = 2$  mode visualization, distinct elongated structures are present throughout the domain. Notice in particular the structures inside the dashed rectangular boxes. The streamwise extent of these structures can be up to  $\lambda_x/D \approx 25$  (see  $70 < x/D < 95$ ), significantly larger than the wavelength of the vortex shedding mode  $\lambda_x/D \approx 7$ .

Figure 2(a,c) show the instantaneous streamwise velocity field in the near-intermediate and intermediate-far wake, respectively, of the disk on a  $x/D - \theta$  plane. The  $x/D - \theta$  plane is constructed by unrolling the cylindrical surface at a constant  $r/D$ . For the near-intermediate field (figure 2a), the plane is located at  $r/D = 1.25$  while for the intermediate-far field (figure 2c),  $r/D = 2.5$  is chosen. In both figures, vortex shedding structures are evident, spaced at an approximate wavelength of  $\lambda_x/D \approx 7$ . These structures and the wavelength of  $\lambda_x/D \approx 7$  become even more evident when the flow field at the respective radial locations in the near-

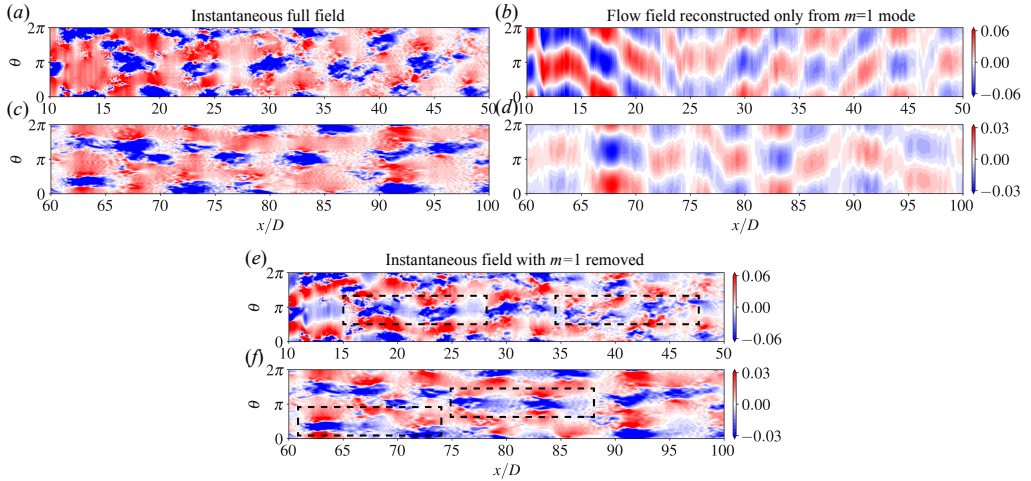


Figure 2: Instantaneous streamwise velocity on  $x/D - \theta$  planes at  $r/D = 1.25$  (a,b,e) and  $r/D = 2.5$  (c,d,f). Panel (a,c) shows the full streamwise velocity field. Panel (b,d) shows the field reconstructed from  $m = 1$  contribution only. Panel (e,f) shows the field with  $m = 1$  contribution removed. Rectangular boxes in (e, f) emphasize the large-scale streaks in the flow field with the  $m = 1$  mode removed.

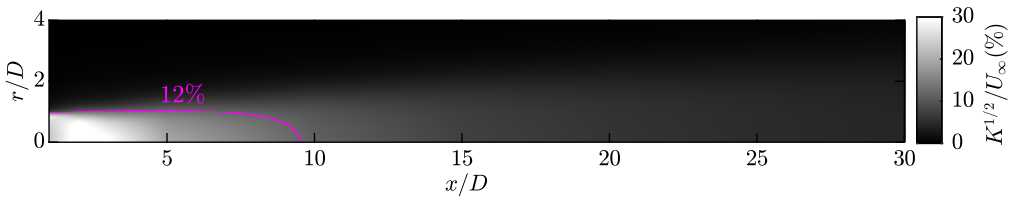


Figure 3: Turbulence intensity ( $K^{1/2}/U_{\infty}$ ) as a function of streamwise ( $x$ ) and radial ( $r$ ) directions. Magenta curve demarcates the region where  $K^{1/2}/U_{\infty}$  reduces to 0.12.

intermediate and intermediate-far wake are constructed with only the  $m = 1$  mode, as shown in figure 2(b, d). Upon removing the contribution of the vortex shedding mode that lies in  $m = 1$  azimuthal wavenumber (Johansson *et al.* 2002; Johansson & George 2006; Nidhan *et al.* 2020), the streaks become readily apparent in figure 2(b,d). See again the structures contained inside dashed rectangular boxes in figure 2(b,d). These observations in figure 1 and 2 are strong initial indications of the presence of large-scale streaks in turbulent wakes, similar to those recently reported in the numerical and experimental datasets of turbulent jets (Pickering *et al.* 2020; Nogueira *et al.* 2019). In what follows, the characteristics and robustness of these elongated structures are quantified through various statistical and spectral measures.

To this end, we invoke the Taylor's hypothesis, converting time  $t$  at a location  $x_0$  to pseudo-streamwise distance from  $x_0$ :  $x_t = U_{\text{conv}}t$ , where  $U_{\text{conv}} = U_{\infty} - U_d$  is the convective velocity. Since the defect velocity in the wake  $U_d \ll U_{\infty}$  (where  $U_{\infty}$  is the free-stream velocity),  $U_{\text{conv}}$  is approximated by  $U_{\infty}$ . Taylor's hypothesis requires velocity fluctuation to be sufficiently small compared to  $U_{\text{conv}}$ . Figure 3 shows that this requirement is met since turbulence intensity ( $K^{1/2}/U_{\infty}$ ) drops below 12% beyond  $x/D = 10$  for all radial locations and below 4% at  $x/D = 30$ . Previous work on turbulent wakes has shown Taylor's hypothesis to be valid in the wake when  $K^{1/2}/U_{\infty}$  drops below  $\sim 10\%$  (Antonia & Mi 1998; Kang &



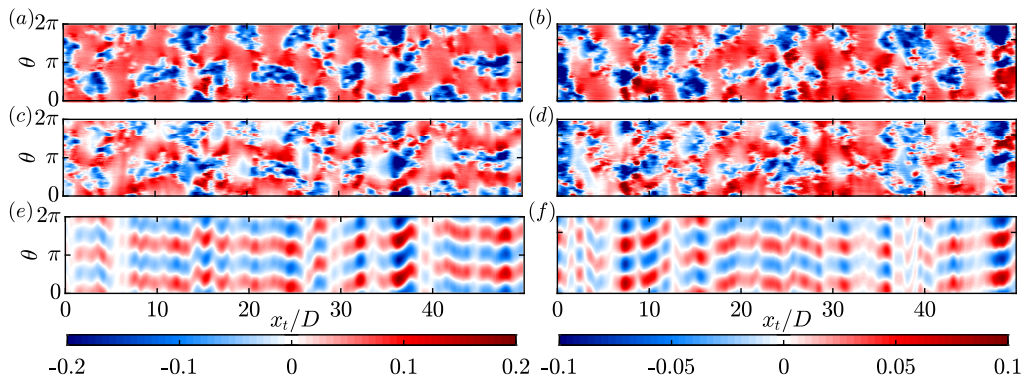


Figure 4: Streamwise velocity fluctuations  $u'_x$  on a  $x_t/D$ - $\theta$  plane at  $r/D \approx 0.8$ : (a, c, e)  $x_0/D = 10$ ; (b, d, f)  $x_0/D = 20$ . Top row (a, b) include all azimuthal components, middle row (c, d) excludes  $m = 1$ , and the bottom row (e, f) includes solely  $m = 2$ .

Meneveau 2002; Dairay *et al.* 2015; Obligado *et al.* 2016). Invoking Taylor's hypothesis,  $St \approx U_\infty k_x$ . In this study we will particularly focus on  $St \rightarrow 0$  (obtained from either temporal spectra or SPOD at different  $x/D$  locations) which, by Taylor's hypothesis, is equivalent to large-scale streaks with  $k_x \rightarrow 0$  ( $k_x$  being the streamwise wavenumber) at those locations.

In figure 4, the near-to-intermediate wake behavior is shown at  $x_0/D = 10$  (left column) and 20 (right column) through plots of streamwise velocity fluctuation ( $u'_x$ ) at  $r/D = 0.8$  in the  $x_t/D - \theta$  plane. Time  $t$  is transformed to the  $x_t$  coordinate by application of Taylor's hypothesis, which is valid beyond  $x/D \geq 9$  in the wake, as was shown through figure 3 and the associated discussion.

Due to the strong signature of the vortex shedding mode in the near to intermediate wake, alternate patches of inclined positive and negative fluctuations separated by  $\lambda_D \approx 1/St_{VS}$  dominate the visualization in figure 4(a, b). It is known *a priori* that these structures are contained in the  $m = 1$  azimuthal mode. In order to assess space-time coherence other than the vortex shedding mode, the streamwise fluctuations are replotted in figure 4(c, d) after removing the  $m = 1$  contribution. Once the  $m = 1$  contribution is removed, streamwise streaks become evident at both locations. Furthermore, one can also observe that these streaks appear to be primarily contained in the azimuthal mode  $m = 2$ , i.e, there are two structures over the azimuthal length of  $2\pi$ . Only the  $m = 2$  component is shown in figure 4(e, f) and, on doing so, the elongated streamwise streaks come into sharper focus. Building upon figure 1, figure 4 (c, d, e, f) lend support to the spatiotemporal robustness of these large-scale streaks in the turbulent wake of circular disk.

The downstream distance ( $0 < x/D < 120$ ) spanned in the simulations of Chongsiripinyo & Sarkar (2020) is very large, thus enabling the far field to be probed too for the presence (or absence) of the streamwise streaks. Figure 5(a, c) show the  $x_t/D - \theta$  plots of  $u'_x$ , with contribution of  $m = 1$  mode excluded, in regions starting at  $x_0/D = 40$  and 80. The  $x_t/D - \theta$  planes are located at  $r/D = 2$  for these far-wake locations since the wake width grows with  $x$ . Interested readers can refer to figures 5, 15, 16 of Chongsiripinyo & Sarkar (2020) and figure 5 of Nidhan *et al.* (2020) for an in-depth discussion about the mean and turbulence statistics. Similar to the near wake plot in figure 4(c, d), large-scale streaks elongated in the streamwise direction are found to extend into the far wake as well. Once again, isolating

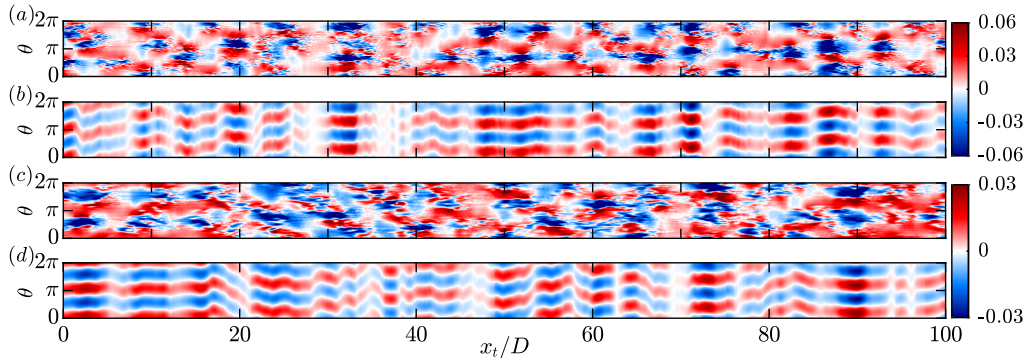


Figure 5: The  $u'_x$  field on a  $x_t/D$ - $\theta$  plane at  $r/D \approx 2.0$ : (a,b)  $x_0/D = 40$ ; (c,d)  $x_0/D = 80$ . In (a,c)  $m = 1$  is removed and in (b,d) only  $m = 2$  is shown.

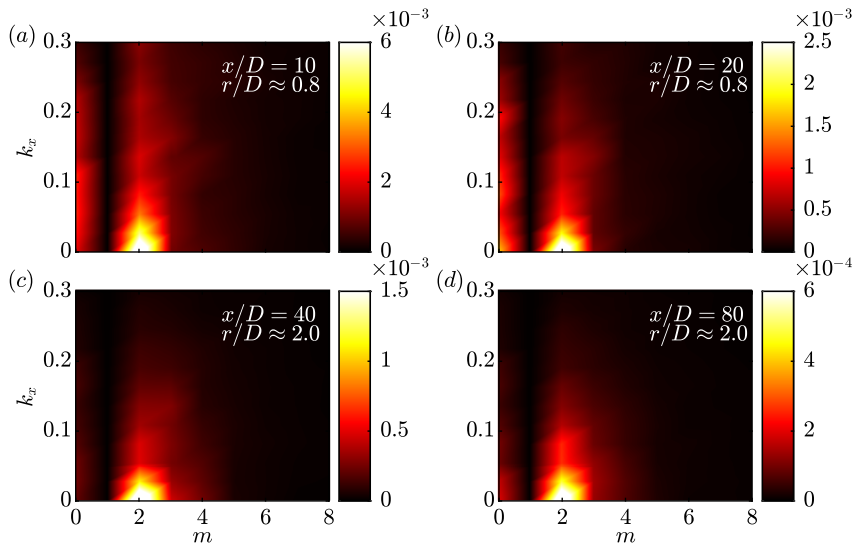


Figure 6: 2D power spectral density of the streamwise velocity fluctuation in  $(k_x, m)$  space: (a)  $x/D = 10$ ,  $r/D \approx 0.8$ ; (b)  $x/D = 20$ ,  $r/D \approx 0.8$ ; (c)  $x/D = 40$ ,  $r/D \approx 2.0$ ; (d)  $x/D = 80$ ,  $r/D \approx 2.0$ . The  $m = 1$  wavenumber is removed so as to de-emphasize the vortex-shedding structure.

the  $m = 2$  component (figure 5b and d) highlights the streaks. Collectively, figures 4, and 5 demonstrate that the streaks span the entire wake length and that the  $m = 2$  mode drives these streaks.

Figure 6 shows two-dimensional (2D) spectra in the streamwise wavelength ( $k_x$ ) – azimuthal mode ( $m$ ) space at four representative streamwise locations  $x/D = 10, 20, 40$ , and 80. Here,  $k_x$  is the wavenumber of the pseudo-streamwise direction  $x_t$ . The  $m = 1$  contribution is removed *a priori* to emphasize the large-scale streaks. At all these four locations, these streaky structures correspond to  $k_x \rightarrow 0$  and are found to reside in the  $m = 2$  azimuthal mode. Note that the  $k_x = 0, St = 0$  should be interpreted as  $k_x, St \rightarrow 0$  as the length of the time series is not sufficient to resolve the large time-scale of streaks. In appendix A, we vary the spectral estimation parameter  $n_{\text{fit}}$  to resolve the lower frequencies and identify the frequency associated with streaks in this limit to be around  $St \approx 0.006$ .

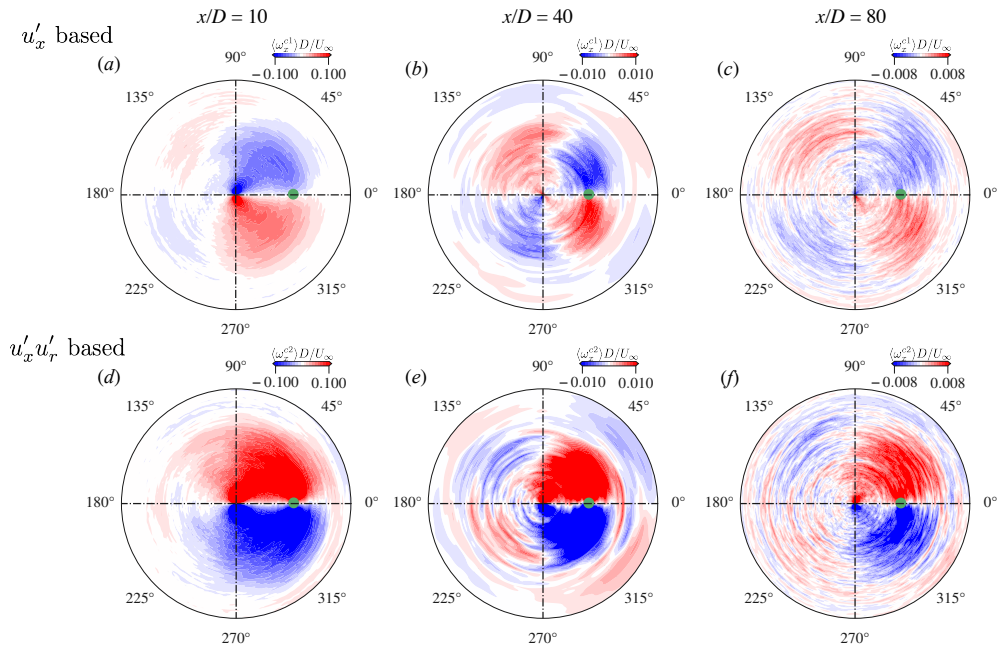


Figure 7: Conditionally-averaged streamwise vorticity at  $x/D = 10$  (left column), 40 (middle column) and 80 (right column). Top row (a, b, c) shows  $\langle \omega_x^{c1} \rangle$ , conditioned using  $u'_x$  and bottom row (d, e, f) shows  $\langle \omega_x^{c2} \rangle$ , conditioned using  $u'_x u'_r$ . Green dot shows the location of conditioning point – (a, d)  $r/D \approx 0.8, \theta \approx 0^\circ$  and (b, c, e, f)  $r/D \approx 2, \theta \approx 0^\circ$ . Radial domain extends until  $r/D = 2$  at  $x/D = 10$  and until  $r/D = 5$  at  $x/D = 40, 80$ . Positive vorticity (red) is out of the plane and negative vorticity (blue) is into the plane.

### 3.2. Evidence of lift-up mechanism in the wake

Previous work in turbulent free shear flows and wall-bounded flows often attribute the formation of streaks in the velocity to the lift-up mechanism (Ellingsen & Palm 1975; Landahl 1975). The lift-up mechanism, by sweeping fluid from high-speed regions to low-speed regions and vice versa, leads to the formation of high-speed and low-speed streaks, respectively. Brandt (2014) provides a comprehensive review of the lift-up mechanism and its crucial role in various fundamental phenomena, e.g., subcritical transition in shear flows, self-sustaining cycle in wall bounded flows, and disturbance growth in complex flows.

To investigate the presence of the lift-up mechanism in the wake, we plot conditional averages of streamwise vorticity fluctuations ( $\omega_x$ ) at three representative locations in the flow – the planes,  $x/D = 10, 40$  and  $80$  in figure 7. The top row shows a conditional average,  $\langle \omega_x^{c1} \rangle$ , designed to extract the structure of the streamwise vorticity on a constant- $x$  plane during times of large streamwise velocity fluctuations. Specifically, the condition is that

$$u'_x \geq c(u'_x)^{\text{rms}}, \quad (3.1)$$

at a specified point P on that plane, and  $\langle \omega_x^{c1} \rangle$  is the temporal average of all  $\omega_x(t)$  that satisfies this condition. The conditional point P (shown as green dots in figure 7) is chosen to lie at  $\theta = 0$  and radial locations of  $r/D = 0.8$  and  $2$  for  $x/D = 10$  and  $x/D = 40, 80$ , respectively. The selection of different radial locations at  $x/D = 10$  and  $x/D = 40, 80$  is based on the approximate values of mean wake half-widths at the respective  $x/D$  locations (Chongsiripinyo & Sarkar 2020). Owing to rotational invariance of statistics for an axisymmetric wake, the condition is applied to a new point P<sub>1</sub> at the same  $r/D$  but a

different value of  $\theta$  and the new  $\langle \omega_x^{c1} \rangle$  field, after a rotation to bring  $P_1$  to  $P$ , is included in the conditional average. Since  $N_\theta = 256$  points is used for discretization, the ensemble used for the conditional average is significantly expanded by exploiting rotational invariance of statistics. The bottom row of figure 7 shows  $\langle \omega_x^{c2} \rangle$  computed using a different condition at point  $P$ ,

$$-u'_x u'_r \geq c (-u'_x u'_r)^{\text{rms}}. \quad (3.2)$$

This condition is designed to identify the structure of streamwise vorticity at times of significant Reynolds shear stress at point  $P$ . The results exhibit moderate sensitivity to  $c \in (0, 1]$  as reported in appendix B. Hence,  $c$  is set to 0.5 as a compromise between identification of intense events and retention of sufficient snapshots for conditional averaging.  $(u'_x)^{\text{rms}}$  and  $(-u'_x u'_r)^{\text{rms}}$  are the r.m.s. values of the streamwise velocity fluctuations and the r.m.s. values of the streamwise-radial fluctuations correlation at the conditioning points, respectively.

The conditionally averaged field based on equation (3.1) captures the structure of the streamwise vorticity field during events of intense positive  $u'_x$ . In figure 7(a), two rolls of streamwise vorticity are observed in the conditionally averaged field: negative on the top and positive at the bottom of the conditioning point, respectively. These streamwise vortex rolls push the high-speed fluid in the outer wake to the low-speed region in the inner wake around the conditioning points (green dot), leading to  $u'_x > 0$ . When the averaging procedure is conditioned on negative streamwise velocity fluctuations, i.e.,  $u'_x \leq -c(u'_x)^{\text{rms}}$ , the signs of the vortex rolls in figure 7 are interchanged, as expected (figure not shown). At  $x/D = 40$  and 80 (figure 7b, c), two additional vortical structures are observed in the  $\theta = [90^\circ, 270^\circ]$  region. However, around the conditioning point the spatial organization of vorticity remains qualitatively similar. The size of these vortex rolls increase with  $x/D$ , consistent with the radial spread of wake.

The conditionally averaged field based on equation (3.2) captures the vorticity field corresponding to intense positive  $-u'_x u'_r$  values. In a turbulent wake,  $-u'_x u'_r$  is predominantly positive such that the dominant production term in the wake,  $P_{xr} = \langle -u'_x u'_r \rangle \partial U / \partial r > 0$ , acts to transfer energy from the mean flow to turbulence. Now turning to equation (3.2), positive  $-u'_x u'_r$  can result from two scenarios: (a) ( $u'_r > 0, u'_x < 0$ ), i.e., ‘ejection’ of low-speed fluid from the inner wake to the outer wake and (b) ( $u'_r < 0, u'_x > 0$ ), i.e., ‘sweep’ of high-speed fluid from outer wake to the inner wake. Both of the above-mentioned scenarios are consistent with the lift-up mechanism. If ejection and sweep events were equally probable,  $\langle \omega_x^{c2} \rangle \approx 0$  due to the opposite spatial distribution of vortices during ejection and sweep events. However,  $\langle \omega_x^{c2} \rangle$  obtained from  $-u'_x u'_r$  based conditioning (bottom row of figure 7) shows that the positive and negative vortices are spatially organized such that the flow induced by these vortices at the conditioning point is outward ( $u'_r > 0$ ), pushing low-speed fluid from the inner wake to the outer wake. In short,  $\langle \omega_x^{c2} \rangle$  fields in the bottom row of figure 7 correspond to the ejection events at the conditioning point. A similar spatial organization of  $\langle \omega_x^{c2} \rangle$  is observed across the wake cross-section when the radial location of the conditioning point is varied (plots not shown for brevity). This observation establishes that ejections are the dominant contributors to intense positive  $-u'_x u'_r$ , as opposed to sweep events, and therefore, ejections are more instrumental in the energy transfer from mean to turbulence. Previous studies (Wallace 2016; Kline *et al.* 1967; Corino & Brodkey 1969) of the turbulent boundary layer have also reported that ejection events are the primary contributors to Reynolds shear stress.

Figure 7 has two important implications. First, the top row demonstrates strong correlation between intense  $u'_x$  fluctuations and distinct streamwise vortical structures, indicating that the lift-up mechanism is active in the turbulent wake, both in the near field as well as the

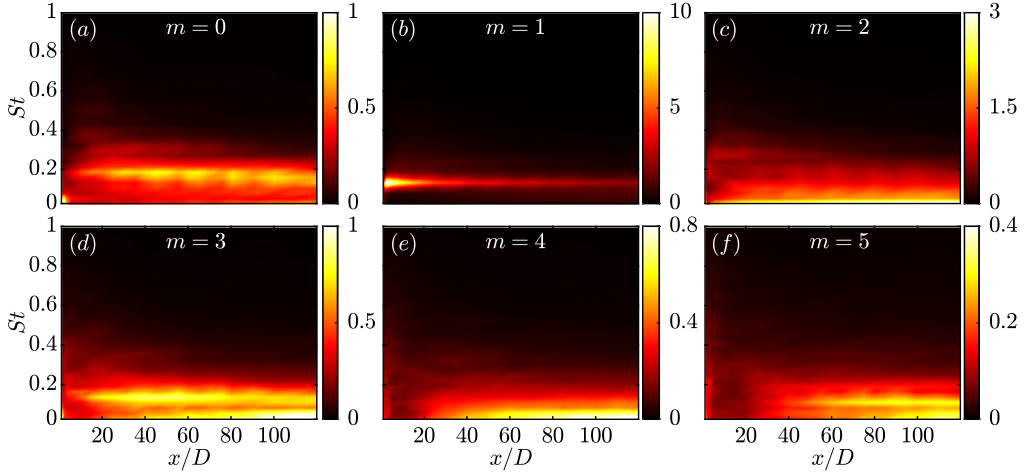


Figure 8: Percentage of energy contained in the leading SPOD modes,  $\lambda^{(1)}$ , as a function of frequency  $St$  and streamwise location  $x/D$  at different azimuthal wavenumbers: (a)  $m = 0$ ; (b)  $m = 1$ ; (c)  $m = 2$ ; (d)  $m = 3$ ; (e)  $m = 4$ ; (f)  $m = 5$ . The leading SPOD eigenvalue,  $\lambda^{(1)}(St, x/D)$ , is normalized with the total TKE  $E_k^T(x/D)$  at the corresponding streamwise location to calculate the percentage contribution.

far field. Second, the conditionally averaged fields obtained using  $u'_x u'_r$  inform us that the lift-up mechanism corresponding to the ejection of low-speed fluid from the inner wake to the outer wake is more dominant than the sweep of high-speed fluid from the outer wake to the inner wake. To the best of authors' knowledge, both these observations constitute the first numerical evidence in the near and far field of a canonical bluff-body turbulent wake of (a) the lift-up mechanism and (b) the dominance of ejection events .

#### 4. SPOD analysis of streaks in the wake

§3 reveals the presence of large-scale streaks and also that the lift-up mechanism is active in the wake. Furthermore, the  $m = 2$  azimuthal wavenumber visually appears to be the dominant streak-containing mode. In this section, SPOD is employed to quantify the energetics and educe the dominant structures of the dominant features at  $St \rightarrow 0$  in the wake. We particularly focus on the  $m = 2$  mode, providing further evidence that these modes exhibit properties of streaks and are formed due to the lift-up mechanism. Direct comparison with the VS mode ( $m = 1, St = 0.135$ ) is provided as appropriate to differentiate the role of streaks from that of the VS mode.

##### 4.1. Energetics of streaky structures using SPOD analysis

SPOD is performed at different streamwise locations ( $x/D$ ) in  $1 \leq x/D \leq 120$ . By definition, the leading SPOD modes at a given  $x/D$  represents the most energetic coherent structures at the associated frequency ( $St$ ) and azimuthal wave number ( $m$ ). Figure 8 shows the percentage of energy in the leading SPOD modes ( $\lambda^{(1)}$ ) as a function of frequency and streamwise distance for the first six azimuthal wavenumbers  $m = 0$  to  $m = 5$ . The percentage of energy at each streamwise location is obtained by normalizing the leading eigenvalue with the total turbulent kinetic energy,  $E_k^T(x/D)$  at the corresponding location. Overall, the most significant contributors to the TKE are the vortex shedding mode ( $m = 1, St = 0.135$ ) and the mode corresponding to streaks ( $m = 2, St \rightarrow 0$ ), as reported in Nidhan *et al.* (2020). The

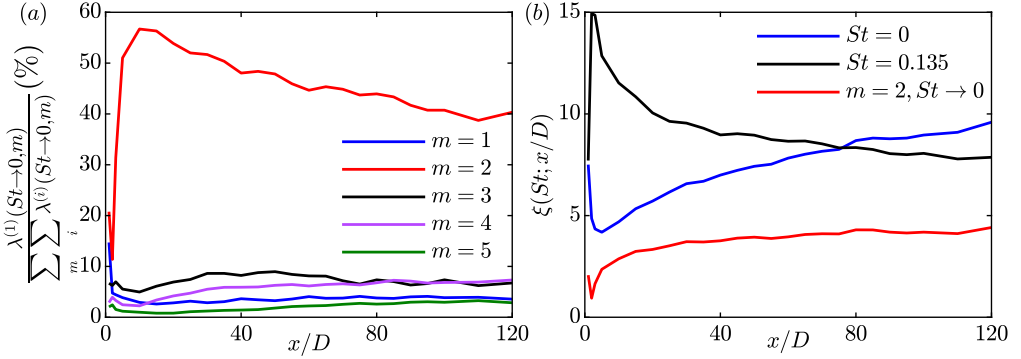


Figure 9: (a) Contribution of the leading SPOD modes  $\lambda^{(1)}$  at different azimuthal wavenumbers to  $St \rightarrow 0$ . (b) Percentage energy contained in the frequencies  $St = 0.135$  and  $St \rightarrow 0$ .

leading vortex shedding SPOD mode contains about 10% energy in the near wake region ( $5 \lesssim x/D \lesssim 15$ ) and decreases thereafter. The leading SPOD mode corresponding to the streaks in the  $m = 2$  mode contains approximately 3% energy from  $x/D = 10$  onward. The axisymmetric component ( $m = 0$ ) exhibits a peak at  $St \rightarrow 0.054$  at  $x/D = 1$  and a much smaller peak at  $St \approx 0.19$  between  $10 \lesssim x \lesssim 120$ . The former is associated with the pumping of the recirculation bubble (Berger *et al.* 1990), whereas the latter was observed in previous studies (see figure 12 in Berger *et al.* (1990) and figure 7 in Fuchs *et al.* (1979b)) but was not investigated further. The  $m = 0$  mode is not the focus of this study.

The energy,  $\lambda^{(1)}$ , contained in the higher azimuthal wavenumbers ( $m = 3 - 5$ ) is shown in figures 8(d-f), respectively. Although  $\lambda^{(1)}$  is smaller than at  $m = 1$  or  $m = 2$ , the higher modes also exhibit temporal structure. The  $m = 3$  component shows energy concentration at the vortex shedding frequency  $St = 0.135$  for  $15 \lesssim x/D \lesssim 70$  and at  $St \rightarrow 0$  for  $x/D \gtrsim 50$ . For  $m = 4$ , energy is concentrated near  $St \rightarrow 0$  for  $x/D \gtrsim 60$ . For the  $m = 5$  component, traces of the vortex shedding mode and streaks ( $St \rightarrow 0$ ) are observed at the streamwise locations  $x/D \gtrsim 60$  and  $x/D \gtrsim 80$ , respectively. Figure 8 indicates that the peaks at the vortex shedding frequency are present only at the odd azimuthal wavenumbers ( $m = 1, 3, 5$ ), whereas the peaks corresponding to the large-scale streaks, i.e.,  $St \rightarrow 0$ , can be found at both the odd and even  $m$ . It is also interesting to note that, for higher  $m$ , both the vortex shedding modes and streaks do not appear until larger values of  $x/D$ . This suggests nonlinear interactions among different frequencies and azimuthal wavenumbers as the wake evolves, as will be elaborated in §5.

The  $St \rightarrow 0$  streaks are dominated by the  $m = 2$  azimuthal wavenumber as demonstrated by figure 9(a), which shows the contribution of different  $m$  at  $St \rightarrow 0$ . The leading eigenvalues of each azimuthal wavenumber is normalized by the total energy at  $St \rightarrow 0$ , i.e.,  $\sum_m \sum_i \lambda^{(i)}(St \rightarrow 0, m)$ . Streaks are azimuthally non-uniform structures and are not present in the axisymmetric  $m = 0$  component. Hence, we focus on  $m \geq 1$ . The azimuthal wavenumber  $m = 2$  is energetically dominant at the  $St \rightarrow 0$  frequency, containing about 40 – 50% of the total energy at  $St \rightarrow 0$ . The sub-optimal wavenumber is  $m = 3$  for  $5 \leq x \leq 80$  and switches between  $m = 3$  and  $m = 4$ , thereafter. However, the difference in energy between the  $m = 2$  and  $m = 3$  wavenumbers is always large,  $>30\%$ . This dominance of the  $m = 2$  wavenumber at  $St \rightarrow 0$  is also consistent with the visualizations of the streamwise velocity fluctuations in figure 4 and figure 5 where one can even see the presence of  $m = 2$  with the naked eye.

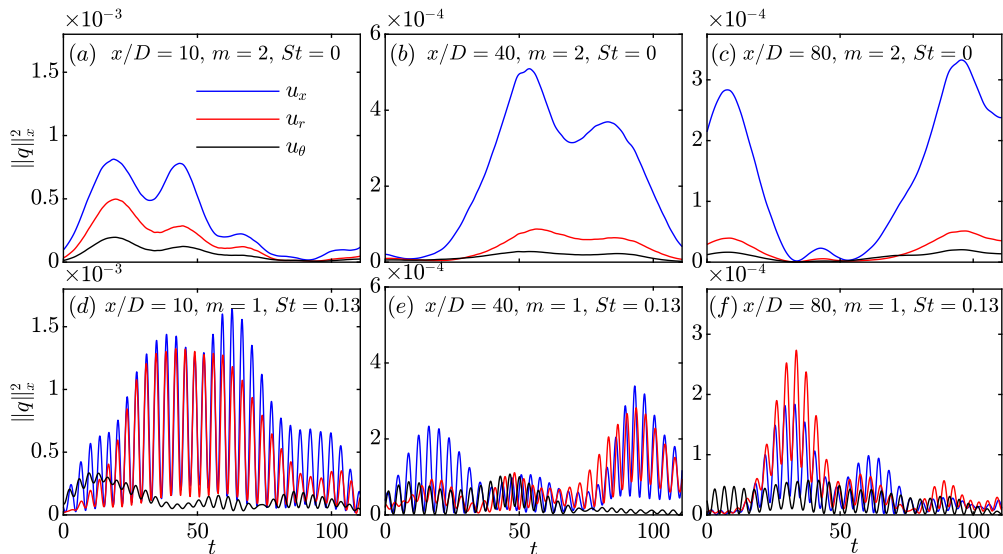


Figure 10: Component-wise instantaneous energy reconstructed from the  $m = 2$  streaky structures in the top row (a-c) and vortex shedding structures (d-f) in the bottom row. The plane integral of the energy is shown at various streamwise locations: (a, d)  $x/D = 10$ , (b, e)  $x/D = 40$  and (c, f)  $x/D = 80$ . Flow reconstruction uses the leading five SPOD modes. The oscillation frequency of the reconstructed energy in (d-f) is twice that of the VS frequency.

The energetic contribution of the two dominant frequencies,  $St = 0.135$  (vortex shedding) and  $St \rightarrow 0$  (streaks), is compared by computing the percentage of total energy (across all  $m$  and  $i$ ) at a given frequency  $St$  as

$$\xi(St; x/D) = \frac{\sum_m \sum_i \lambda^{(i)}(m, St; x/D)}{E_k^T(x/D)} \times 100. \quad (4.1)$$

Figure 9(b) shows that the vortex shedding frequency is more dominant in the region  $x \leq 70$ , whereas the zeroth frequency dominates for  $x \geq 70$ . This implies that although the streaks are present throughout, they are energetically more prominent in the far wake region. It is interesting to note that beyond  $x/D \approx 65$ , the defect velocity decay rate changes from  $x^{-1}$  to  $x^{-2/3}$  in the wake (Chongsiripinyo & Sarkar 2020). For comparison, the most dominant component at the zeroth frequency, i.e.,  $m = 2$  is also shown in figure 9(b), which exhibits a similar trend of increasing prominence in the downstream direction.

Having diagnosed the streaky structure ( $m = 2, St \rightarrow 0$ ) and the vortex shedding structure ( $m = 1, St = 0.135$ ) using SPOD, we shift focus to their imprint on the flow in physical space by reconstructing the flow field using their leading five SPOD modes. The  $m = 2$  wavenumber is selected because it is energetically dominant at  $St \rightarrow 0$ . The reconstruction is performed using the convolution strategy described in section §2. Figure 10(a,b,c) shows the instantaneous energy in the three fluctuation components,  $u'_x$ ,  $u'_r$ , and  $u'_\theta$  at  $x/D = 10, 40$ , and  $80$ , after reconstruction with the streaky-structure SPOD modes. The instantaneous energy is depicted within the time interval  $t \in [0, 110]$ , which corresponds to the first five blocks used for SPOD, and is representative of the entire reconstructed flow fields. The energy of  $u'_x$  is significantly higher than that of  $u'_r$  and  $u'_\theta$ . The dominance of the streamwise component over its radial and azimuthal counterparts is one salient feature of

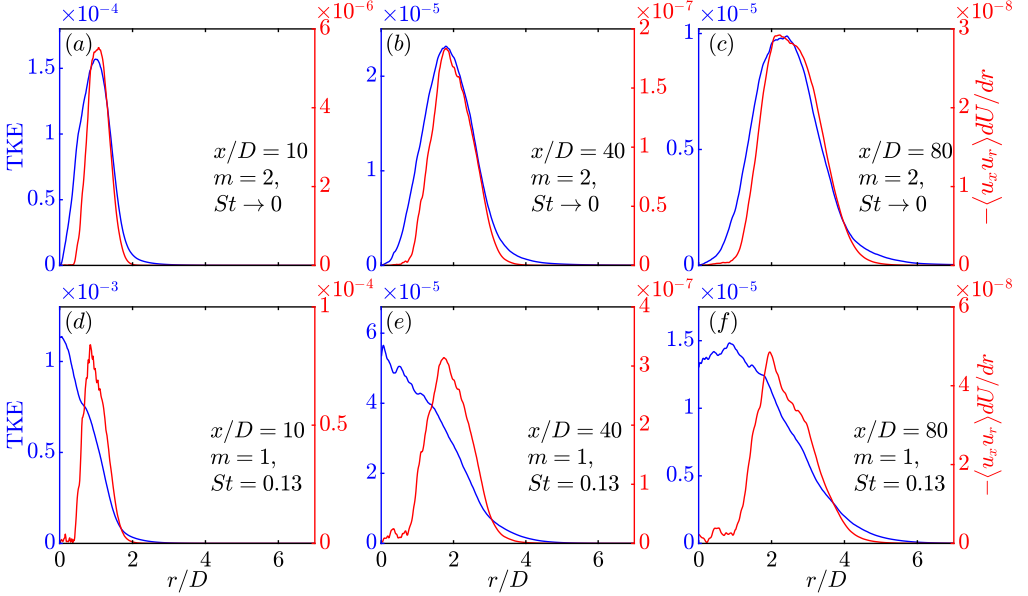


Figure 11: TKE and production due to shear at different downstream locations for the flow fields reconstructed from the streaky-structures mode in the top row (a-c) and VS mode in the bottom row (d-f). Left column (a, d) corresponds to  $x/D = 10$ , middle column (b, e) to  $x/D = 40$  and right column (c, f) to  $x/D = 80$ . Flow reconstruction uses the leading five SPOD modes.

streaks. The finding of  $u'_x$  dominance is in agreement with those of Boronin *et al.* (2013, see figure 11) and Pickering *et al.* (2020, see figure 10) in the context of round jets, indicating similarity in streak formation between jets and wakes. The lift-up mechanism, in which the streamwise vortices lift up and push down the low-speed and high-speed fluid, respectively, is responsible for elongated streaks accompanied by an amplification of  $u'_x$ . The analog of panels in figure 10(a-c) is shown for the VS mode in panels of figure 10(d-f). Here,  $u'_x$  and  $u'_r$  components have comparable energy, showing a fundamental difference between the vortex shedding mode and the streaky-structures mode as to how each mode contributes to velocity fluctuations in the wake. Furthermore, the instantaneous energy of the flow field reconstructed from the VS mode has a much smaller time scale in comparison to that of the large-scale streaks.

Figure 11 shows the TKE ( $K = \langle u'_i u'_i \rangle / 2$ ) and its shear production ( $P_{xr} = -\langle u'_x u'_r \rangle \partial U / \partial r$ ) corresponding to the large-scale streaks and vortex shedding structures at  $x/D = 10, 40$  and  $80$ . As in figure 10, TKE and  $P_{xr}$  are computed from the leading five SPOD modes. Figure 11(a-c) show that the TKE and the production peak at the similar radial location for  $m = 2, St \rightarrow 0$ . This is not the case for  $m = 1, St = 0.135$  (figure 11b-f) where the peak TKE occurs close to the centerline while the production peaks away from the centerline. This difference in the locations of peak  $K$  and  $P_{xr}$  indicates that turbulent transport plays an important role in distributing the TKE in the vortex shedding mode, similar to its importance in the full TKE budget of an axisymmetric wake (Uberoi & Freymuth 1970). The difference in radial locations of peak  $K$  and  $P_{xr}$ , as demonstrated in figure 11, is another crucial distinction between the large-scale streaky mode and the vortex shedding mode. The presence of streaks is associated with high TKE around the region of high production/mean shear indicating their important role in the energy transfer from mean to fluctuation velocity in the turbulent



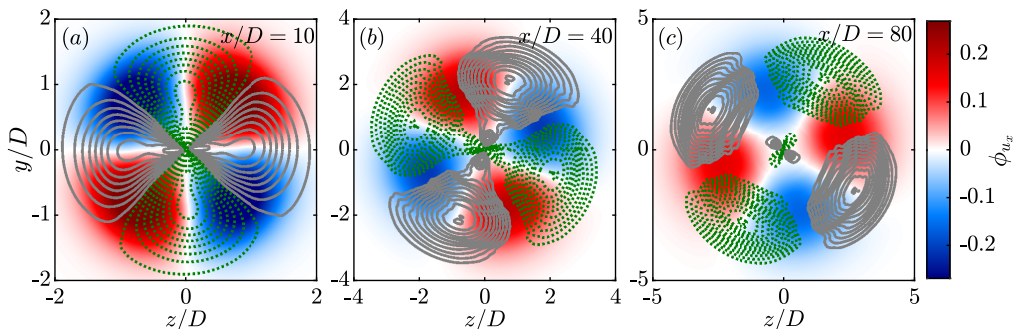


Figure 12: Leading SPOD mode of  $m = 2$  and  $St \rightarrow 0$ : (a)  $x/D = 10$ ; (b)  $x/D = 40$ ; (c)  $x/D = 80$ . The false colors represent the real part of the streamwise velocity component

$\text{Re}[\phi_{u_x}^{(1)}(St \rightarrow 0)]$  and the grey and green-dotted lines correspond to positive and negative streamwise vorticity  $\text{Re}[\phi_{\omega_x}^{(1)}(St \rightarrow 0)]$ , respectively.

wake, similar to other shear flows (Gualtieri *et al.* 2002; Brandt 2007; Jiménez-González & Brancher 2017). As a result, the TKE achieves its global maximum around the same location as that of  $P_{xr}$  for streaks.

#### 4.2. Lift-up mechanism through the lens of SPOD analysis

§4.1 demonstrated that the structures associated with  $St \rightarrow 0$  exhibit the characteristics of streaks and their significance increases from the near to far wake, with the azimuthal wavenumber  $m = 2$  being the most significant, energetically, to the streaks. Figure 12 shows the leading SPOD mode of the streamwise velocity fluctuation ( $u'_x$ ) corresponding to  $m = 2$  and  $St \rightarrow 0$  at three streamwise locations  $x/D = 10, 40,$  and  $80$ . Overlaid on the  $u'_x$  contour is the streamwise vorticity ( $\omega'_x$ ) of the corresponding mode. Both  $u'_x$  and  $\omega'_x$  are characterized by four lobes of alternate sign, the size of which increase monotonically with  $x/D$ . Importantly, the set of  $\omega'_x$  lobes is shifted with respect to the  $u'_x$  lobes by a clockwise rotation of approximately  $45^\circ$ . As a result of the shift, the maximum of  $u'_x$  in the mode appears at the location where the vortices bring in high-speed fluid from the outer to the inner wake, and vice versa. This observation further confirms the presence of lift-up mechanism in the wake.

Figure 13(a) shows the normalized radial profiles of mean defect velocity ( $U_d$ ) at  $x/D = 10, 40$  and  $80$ . Figure 13(b) shows the radial profile of the normalized leading SPOD mode's streamwise component for  $m = 2, St \rightarrow 0$ , at the same streamwise locations as in figure 13(a). As the wake develops in the  $x$  direction, the location of mode maximum shifts away from the centerline. A visual comparison shows that the location of mode maximum (dashed lines in figure 13b) of the dominating streak-containing mode lies in close proximity to the location of the maximum mean shear (dotted-dashed lines in figure 13a). The large radial gradient of the streamwise velocity induces a positive mean vorticity, lifting up the low-speed fluid from the inner wake to form streaks. Hence, an extremum in  $u'_x$  appears in the SPOD mode. The seminal work of Ellingsen & Palm (1975) demonstrates that, for linearized disturbances in an inviscid flow,  $\partial u_x / \partial t \propto -u_r \partial U(r) / \partial r$ , and the lift-up mechanism is most active in the region closest to the largest mean shear. So is the case in the present turbulent wake.

The lift-up mechanism is also active at higher azimuthal wavenumbers as demonstrated

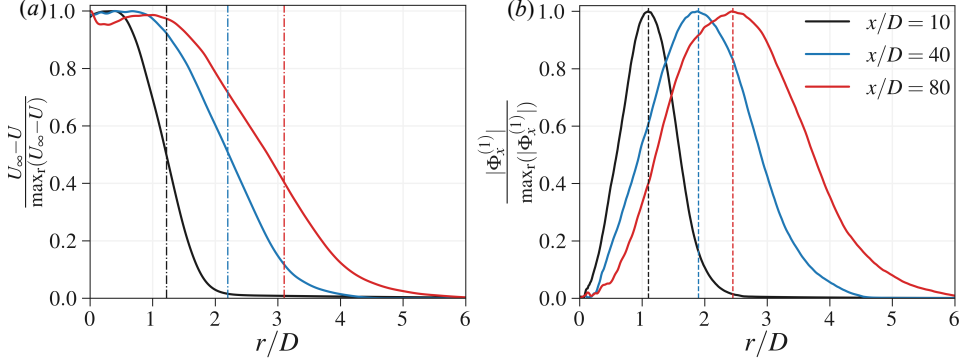


Figure 13: (a) Normalized mean defect velocity ( $U_d = U_\infty - U$ ) profiles. (b) Normalized leading SPOD mode of the streamwise velocity ( $u_x$ ) at  $m = 2$  and  $St \rightarrow 0$ . Dashed lines in (a) and dotted-dashed lines in (b) correspond to the radial location of the maximum of SPOD mode and the maximum of mean shear ( $\partial U / \partial r$ ), respectively.

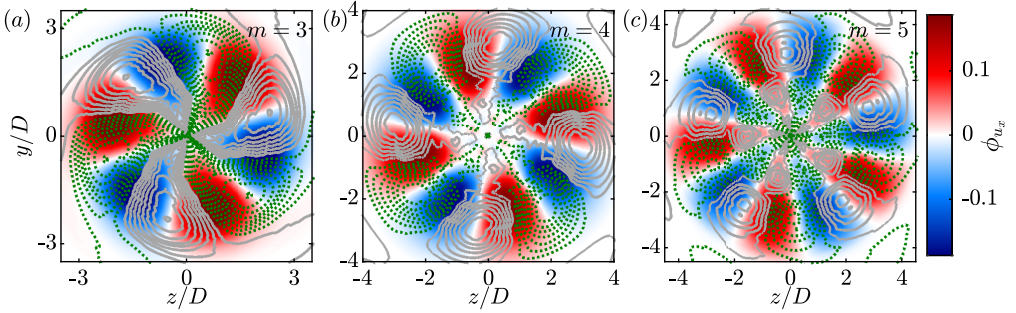


Figure 14: Leading SPOD mode at  $x/D = 40$  and  $St \rightarrow 0$  for higher azimuthal wavenumbers: (a)  $m = 3$ ; (b)  $m = 4$ ; (c)  $m = 5$ . The false colors represent  $\text{Re}[\phi_{u_x}^{(1)}(St \rightarrow 0)]$  and the grey and green-dotted lines correspond to the positive and negative values of streamwise vorticity  $\text{Re}[\phi_{\omega_x}^{(1)}(St \rightarrow 0)]$ .

by figure 14, which shows the leading SPOD modes at  $x/D = 40$  and frequency  $St \rightarrow 0$  for the higher modes:  $m = 3, 4$  and  $5$ . Similar to figure 12, positive and negative streamwise velocity contours are encompassed by counter-rotating vortices that move the fluid from the fast- to slow-speed regions and vice-versa. The radial spread of the streamwise velocity lobes increases with  $m$  and the number of lobes scales as  $2m$ . Also, the vortices are shifted by  $30^\circ$ ,  $22.5^\circ$ , and  $18^\circ$ , for  $m = 3, 4$ , and  $5$ , respectively. In other words, the set of streamwise velocity lobes for wavenumber  $m$  is shifted by an angle of  $\pi/2m$  radians with respect to the streamwise vortices. As in the case of  $m = 2$ , the peak of the leading SPOD modes for  $m = 3, 4, 5$  lies in the vicinity of the maximum mean shear. Even for higher  $m$ , lift-up effect occurs nears the region of the largest mean shear. This further confirms that the lift-up mechanism is active for higher azimuthal wavenumbers.

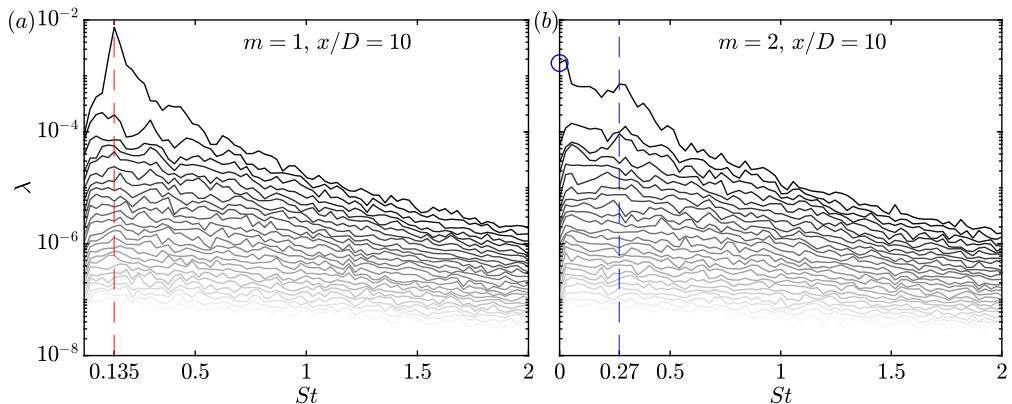


Figure 15: SPOD spectra at  $x/D = 10$ : (a)  $m = 1$ ; (b)  $m = 2$ . Dashed red and blue lines in (a) and (b) correspond to  $St = 0.135$  and  $St = 0.27$ , respectively.

## 5. Analysis of triadic interactions in the wake

Previous sections show that the streaks are predominantly present in the  $m = 2$  azimuthal mode. To shed light on the possible dynamics behind the formation of streaks in a turbulent wake, we focus on the nonlinear interactions between the VS-containing  $m = 1$  mode and the streak-containing  $m = 2$  mode.

### 5.1. Bispectral mode decomposition at select locations

Figure 15 shows the SPOD spectra for the azimuthal wavenumbers,  $m = 1$  and  $m = 2$ , at  $x/D = 10$ . Both SPOD spectra exhibit a large difference between the first and second eigenvalues for  $St \lesssim 0.5$ , thus demonstrating a *low-rank* behaviour. The leading eigenvalue of the  $m = 1$  azimuthal mode peaks at the vortex shedding (VS) frequency,  $St = 0.135$ . On the other hand, the leading eigenvalue of the  $m = 2$  azimuthal mode exhibits a global peak at  $St \rightarrow 0$ , and an additional local peak at  $St = 0.27$  (blue dashed line in figure 15). Furthermore, Nidhan *et al.* (2020, see their figure 20) find that the VS mode gains prominence at  $x/D \approx 1$  while the peak corresponding to  $m = 2, St \rightarrow 0$  appears further downstream at  $x/D \approx 5$ . These observations collectively point towards different sets of triadic interactions involving the VS mode. For example,  $m = 1, St = 0.135$  can interact with  $m = 1, St = -0.135$  to give rise to  $m = 2, St \rightarrow 0$  that appears further downstream. Similarly, the self-interaction of  $m = 1, St = 0.135$  can generate  $m = 2, St = 0.27$  (local peak denoted by dashed line in figure 15b). In what follows, we quantitatively demonstrate that the presence of these triadic interactions at select  $x/D$  locations using bispectral mode decomposition (BMD) (Schmidt 2020).

Figure 16 shows the cross-mode bispectra for the azimuthal wavenumber triad,  $[m_1, m_2, m_3] = [1, 1, 2]$ , at three axial locations,  $x/D = 10, 40$ , and  $80$ . These spectra provide a measure of the interaction among the three azimuthal components. The abscissa ( $St_1$ ) and ordinate ( $St_2$ ) of the BMD spectra correspond to the frequencies of the  $m_1$  mode and  $m_2$  mode, respectively. Here,  $m_1 = 1, m_2 = 1$  and  $m_3 = 2$ . The high-intensity regions in the spectra represent the energetically dominant triads. In figure 16, the mode bispectra are symmetric about the diagonal  $St_1 = St_2$ . At  $x/D = 10$  (figure 16(a)), the most dominant triad is  $(0.135, -0.135, 0.0)$  and other significant triads are  $(0.135, 0.135, 0.27)$  and  $(-0.135, -0.135, -0.27)$ . This observation confirms the presence of triadic interactions hypothesized in the context of figure 15 and emphasizes that the strongest triadic nonlinear interaction is between the VS mode ( $m = 1, St = 0.135$ ), its conjugate ( $m = 1, St = -0.135$ ),

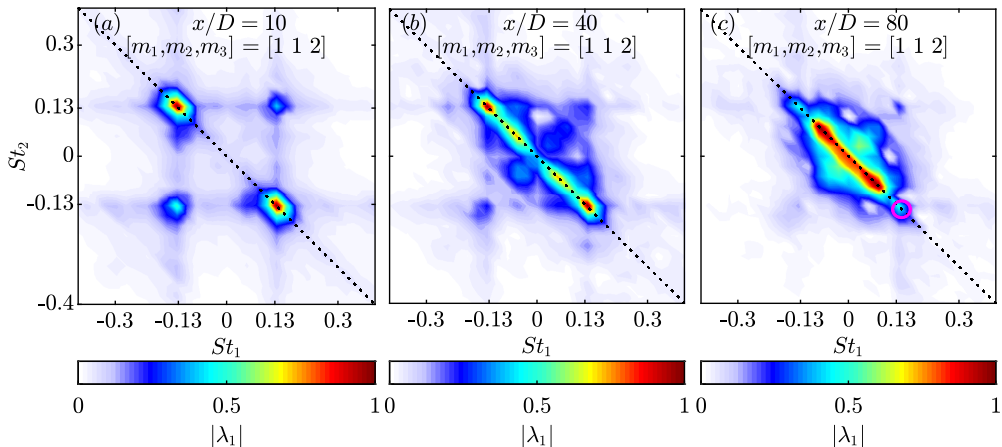


Figure 16: cross-BMD spectra for the azimuthal triad  $[m_1, m_2, m_3 = m_1 + m_2] = [1, 1, 2]$ : (a)  $x/D = 10$ , (b)  $x/D = 40$ , and (c)  $x/D = 80$ . The black dotted line denotes  $St_1 + St_2 = St_3 = 0$ .

and streaks ( $m = 2, St \rightarrow 0$ ). A similar observation is made from the mode bispectra at  $x/D = 40$ . At  $x/D = 80$ , the most dominant triad occurs at  $(0.09, -0.09, 0.0)$  and along the  $St_1 = -St_2$  line, but a local maximum (marked by a circle in magenta) is still present at  $(0.135, -0.135, 0)$ , which indicates that the triadic interaction between the VS mode and its complex conjugate leading to streaks is still active, albeit subdominant. From figure 16, we infer that the triadic interaction between  $[1, 1, 2]$  at  $(0.135, -0.135, 0.0)$  is prominent in the near wake and its intensity progressively decreases downstream. It is important to note that when all interactions with  $[m_1, St_1, m_2, St_2]$  such that  $St_1 + St_2 = 0$  were quantified (not shown here for brevity), that between  $m_1 = m_2 = 1$  and  $St_{1,2} = \pm 0.135$  was found to be the strongest.

Next, we visualize the structures associated with the triadic interaction of the vortex shedding mode, its conjugate, and streaks in figure 17. The real part of the streamwise velocity component of the corresponding cross-bispectral modes is shown at  $x/D = 10, 40$ , and  $80$ . Similar to figure 12, the radial extent of these modes increases downstream and they exhibit four lobes of alternate signs. For a more quantitative comparison, figure 17 (d-f) shows the magnitude of the modes normalized by their maximum value. The corresponding curves are coincident, indicating that the spatial structures generated by the triadic interactions are also the most energetic coherent structures. This further confirms that the  $m = 2, St \rightarrow 0$  mode is indeed generated through the interaction of  $St = \pm 0.135$  at the  $m = 1$  azimuthal mode.

## 5.2. Comparison between nonlinear interactions and linear lift-up mechanism

Finally, the relative role of nonlinear interaction and the linear lift-up mechanism in streak energetics is examined. In figure 18,  $P_{xr}$  denotes shear production in the  $m = 2, St \rightarrow 0$  mode and  $\mathcal{T}_{nl}$  denotes nonlinear energy transfer from  $m = 1, St = \pm 0.135$  modes to the  $m = 2, St \rightarrow 0$  mode. These two terms are defined in appendix C. Figure 18 reveals that both terms are comparable in magnitude and of the same sign for  $x/D \leq 5$ , whereas  $P_{xr}$  dominates beyond  $x/D = 10$ . Thus, near the wake generator, both (a) the nonlinear interaction of the vortex-shedding mode with its conjugate and (b) the linear production due to the lift-up process are of similar importance to streak energetics. Beyond the near wake, the linear mechanism is responsible for maintaining the streaks.

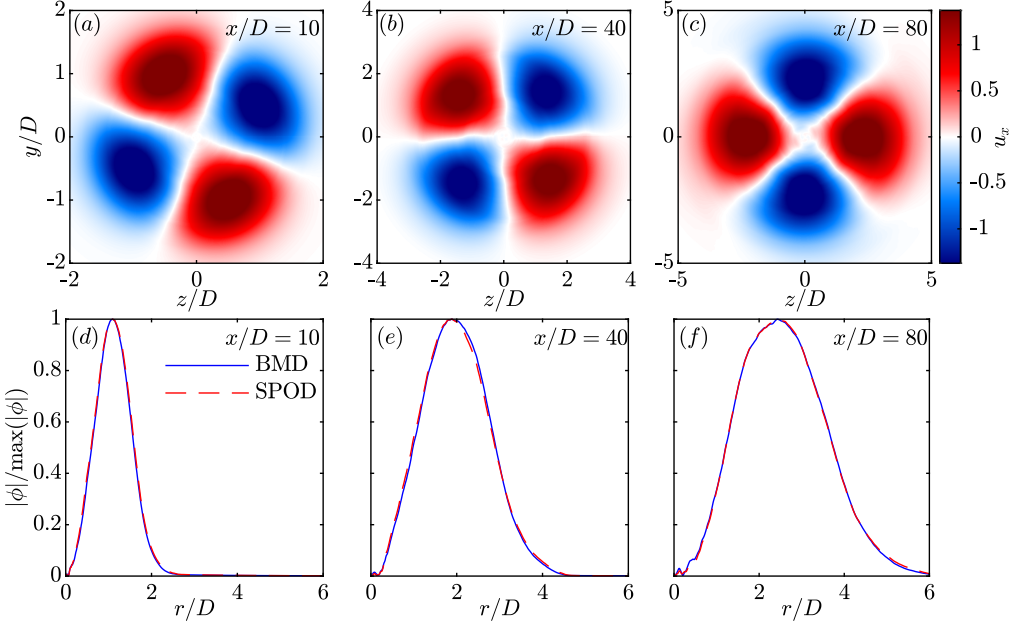


Figure 17: cross-BMD modes for the triad,  $[1, 1, 2]$  in azimuth and  $(0.135, -0.135, 0.0)$  in frequency, at three streamwise locations: (a)  $x/D = 10$ ; (b)  $x/D = 40$ ; (c)  $x/D = 80$ . The false colors represent the real part of streamwise velocity component. The absolute value of the BMD mode and the corresponding leading SPOD mode are compared in (d)-(f).

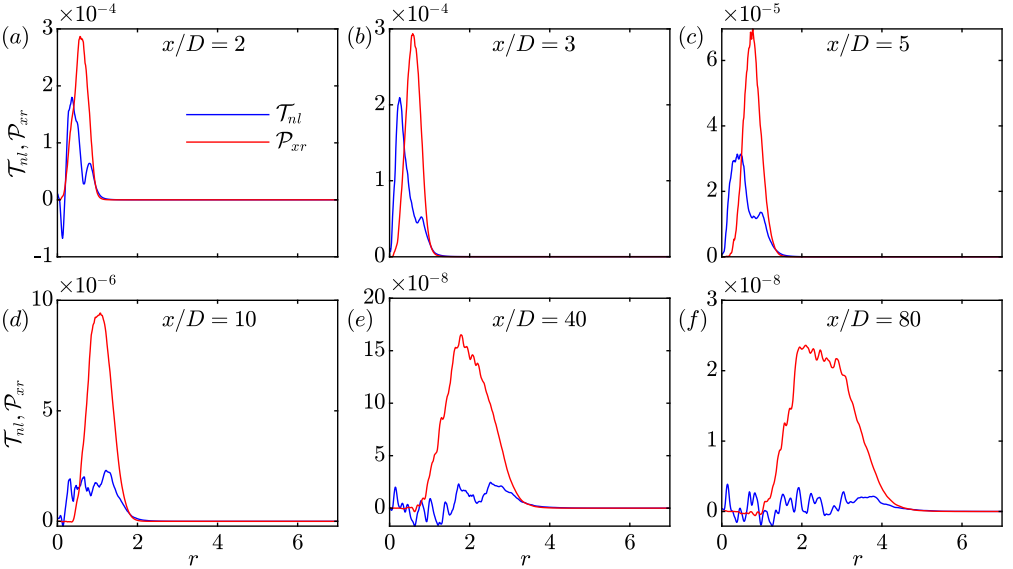


Figure 18: Nonlinear transfer ( $\mathcal{T}_{nl}$ ) from the VS mode and the shear production ( $\mathcal{P}_{xr}$ ) at different streamwise locations for the  $m = 2, St \rightarrow 0$  mode: (a)  $x/D = 2$ ; (b)  $x/D = 3$ ; (c)  $x/D = 5$ ; (d)  $x/D = 10$ ; (e)  $x/D = 40$ ; (f)  $x/D = 80$ .

## 6. Discussions and Conclusions

Streaks, which are coherent elongated regions of streamwise velocity, have been found in a variety of turbulent shear flows. However, they have not received attention in turbulent wakes motivating the present examination of a LES dataset of flow past a disk at  $Re = 50,000$  (Chongsiripinyo & Sarkar 2020). Visualizations and spectral proper orthogonal decomposition (SPOD) are employed and they reveal the presence of streaks from the near wake to the outflow at  $x/D \approx 120$ . Until now, most of the wake literature has understandably focused on the vortex shedding (VS) structure ( $m = 1$ ,  $St = 0.135$  for the circular disk), since it is the energetically dominant coherent structure in the near and intermediate wake. Upon removing the contribution of the  $m = 1$  azimuthal wavenumber *a priori* in visualizations, the streaks become evident, even in the near and intermediate wake. Moreover, in the far wake ( $x/D \geq 70$ ), it is the streaks that become the energetically dominant coherent structure. To the best of our knowledge, this is the first study that reports the existence of streaks in turbulent wakes. These results re-emphasize that mean shear, not a wall boundary condition, is a necessary condition for the existence of streaks (Jiménez & Pinelli 1999; Mizuno & Jiménez 2013; Nogueira *et al.* 2019).

Streaks differ from VS structures in three key ways: (i) they exhibit a much larger wavelength and time scale; (ii) VS structures are tilted with respect to the downstream direction whereas streaks are almost parallel; (iii) the streamwise velocity ( $u'_x$ ) significantly exceeds the other two velocity components ( $u'_r, u'_\theta$ ) in magnitude for streaks whereas  $u'_x$  and  $u'_r$  are comparable for VS structures. The streaky structures are associated with a frequency of  $St \rightarrow 0$  and hence, by Taylor's hypothesis (validated here for the wake) to a wavenumber of  $k_x \rightarrow 0$ . While streaky structures are observed for all non-zero azimuthal wavenumbers,  $m = 2$  dominates in the near-to-far wake. In particular, SPOD analysis reveals that  $m = 2$  contains about 55% (near wake) to 40% (far wake) of the total energy of streaks. This is in contrast to turbulent jets, where Pickering *et al.* (2020) show that the dominant azimuthal wavenumber ( $m_{dom}$ ) at  $St \rightarrow 0$  varies as  $m_{dom} \sim 1/x$  implying that higher  $m$  and not  $m = 2$  would be dominant near the jet nozzle. It is worth noting that only two studies (Johansson & George 2006; Nidhan *et al.* 2020) have reported the importance of  $m = 2$ ,  $St \rightarrow 0$  in turbulent wakes, however they do not link this mode to streaks.

We find that the lift-up mechanism is active in turbulent wakes, similar to wall-bounded shear flows (Abreu *et al.* 2020) and turbulent jets (Lasagna *et al.* 2021; Nogueira *et al.* 2019). Conditional averaging and SPOD analysis clearly demonstrate that streamwise vortices lift up low-speed fluid from the wake's core and push down high-speed fluid from the outer wake. It is also observed that the lift-up mechanism is spatially most active in the vicinity of the largest mean shear and TKE production, indicating that energy is directly transferred from the mean flow to the velocity fluctuations in the streaks. The lift-up process triggered by the streamwise vortices shows a similar energy transfer mechanism in turbulent pipe flow (Hellström *et al.* 2016) and homogeneous shear flow (Gualtieri *et al.* 2002; Brandt 2014).

The lift-up mechanism results in the formation of both low-speed and high-speed streaks. These low- and high-speed streaks exhibit large negative values of Reynolds shear stress. Conditional averaging of streamwise vorticity fluctuations, performed based on peak negative Reynolds shear stress, show that the ejection of low-speed fluid from the wake's core is more dominant than the sweep of the high-speed fluid from the outer wake. The boundary layers also exhibit a similar phenomenon where ejections are a greater contributor to Reynolds shear stress than sweeps (Kline *et al.* 1967; Lu & Willmarth 1973).

Beyond identification of streaks, we also explore the role of nonlinear interactions in the context of wake streaks. Specifically, bispectral mode decomposition (BMD) is used to investigate the nonlinear interactions between the  $m = 1$ ,  $St = \pm 0.135$  VS mode and the

$m = 2$ ,  $St \rightarrow 0$  streak mode. The  $m = 1$ ,  $St = \pm 0.135$  vortices are found to interact and generate the  $m = 2$ ,  $St \rightarrow 0$  vortices. These streamwise vortices of the  $m = 2$ ,  $St \rightarrow 0$  mode then lift up low-speed fluid from the inner wake and push down the high-speed fluid from the outer wake (figure 12) resulting in the formation of streaks. This suggests the wake has a phenomenon analogous to the ‘regeneration cycle’ (Hamilton *et al.* 1995; Farrell & Ioannou 2012) of wall-bounded flows, which involves the generation of streamwise vortices through nonlinear interactions and the formation of streaks through linear advection by these streamwise vortices. Recently, Bae *et al.* (2021) have shown that the nonlinear interactions between spanwise rolls and oblique streaks regenerate streamwise vortices, which then amplify streaks through the lift-up mechanism in wall-bounded flows.

This work demonstrates that streaks and the associated lift-up mechanism are operative in the turbulent disk wake. The results also open directions for future research. Previous work by Ortiz-Tarin *et al.* (2021, 2023) on the wake of a slender 6:1 prolate spheroid found that the wake differs significantly from its bluff-body counterpart. Therefore, one possible direction is to investigate how the shape of the wake generator affects the streaky structures and the lift-up mechanism. Moreover, the influence of the angle of attack and surface properties (roughness, porosity) on the development of these structures could also be explored. Second, it is worth investigating how density stratification (Nidhan *et al.* 2022; Gola *et al.* 2023), often found in the natural environment, affects the lift-up mechanism and formation of streaks in turbulent disk wakes. Lastly, a direct comparison of the characteristics of streaks in wakes, such as length scales, intermittency and life cycle, with those in other turbulent flows such as channel flows and jets can inform us on potentially universal behavior of streaks in turbulent flows. In the same vein, it will be also interesting to build reduced-order models to isolate and understand the spatiotemporal features of interaction between the VS mode and streaks as was done with in a problem with KH-like instabilities and streaks (Nogueira & Cavalieri 2021; Cavalieri *et al.* 2022).

**Acknowledgments.** We thank Dr. K. Chongsiripinyo for the disk wake database.

**Funding.** We acknowledge the support of Office of Naval Research (ONR) grant N00014-20-1-2253.

**Declaration of interests.** The authors report no conflict of interest.

**Author contributions.** A.N. and S.N. have contributed equally to this paper and are co-first authors.

## Appendix A. Effect of parameter, $n_{\text{fft}}$ , on the frequency of the large-scale streaks

Here, the parameter  $n_{\text{fft}}$  is varied to identify the *true* frequency of the streaks in the wake. Due to the constraint of the time-series length, the PSD and SPOD spectra corresponding to the streaks peak in the first frequency bin and are hence interpreted as  $St \rightarrow 0$ . For better resolution, one can increase  $n_{\text{fft}}$ . However, this results in an increase in variance. Hence, we employ the multitaper-Welch based PSD (Thomson 1982) and SPOD (Schmidt 2022) as it outperforms the standard Welch estimator in terms of variance and resolution (Bronez 1992). Recently, Nekkanti & Schmidt (2023) have shown that the parameters,  $n_{\text{fft}}$  and  $n_{\text{ovlp}}$  can significantly affect the spectrum and reconstruction of data. Figure 19 shows the PSD and SPOD performed using  $n_{\text{fft}} = 1024, 2048, 4096$  and  $7132$  with  $N_{\text{win}} = 10$  Slepian tapers as windows. The PSD is computed at  $x/D = 40$ ,  $r/D = 2$  and SPOD spectra at  $x/D = 40$ . As the goal is to identify the true frequency, we plot the spectra for  $St > 0$ . For figure 19 (a,b,e,f), as the  $n_{\text{fft}}$  is not large enough, the peak in the PSD and SPOD is at  $St \rightarrow 0$ . On increasing the  $n_{\text{fft}}$ , two-dimensional PSD and SPOD spectra can resolve the lower frequencies and their peak approaches  $St \approx 0.006$  at the highest possible  $n_{\text{fft}}$  (figure 19d, h). Using this approach, the frequency associated with the large-scale streaky structures can be identified,

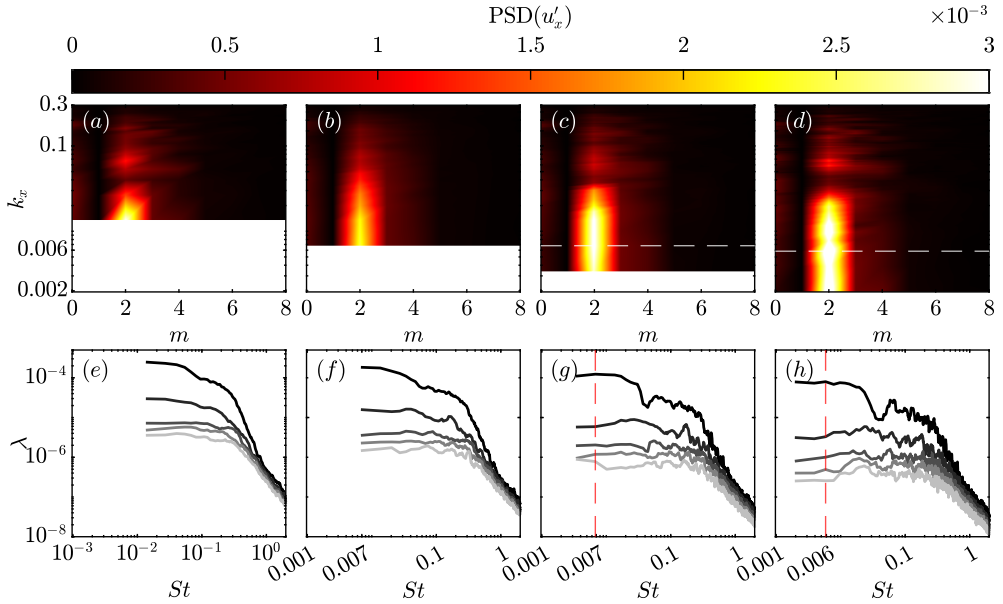


Figure 19: Effect of  $n_{\text{fit}}$  and tapers on the PSD (a-d) at  $r/D = 2$ ,  $x/D = 40$  and SPOD (e-h) at  $x/D = 40$ : (a, e)  $n_{\text{fit}} = 1024$ ,  $N_{\text{win}} = 10$ ; (b, f)  $n_{\text{fit}} = 2048$ ,  $N_{\text{win}} = 10$ ; (c, g)  $n_{\text{fit}} = 4096$ ,  $N_{\text{win}} = 10$ ; (d, h)  $n_{\text{fit}} = 7132$ ,  $N_{\text{win}} = 10$ . The white and red lines in the figure correspond to the peak in PSD and SPOD spectra. The PSD and SPOD spectra are plotted for  $St > 0$ .

which is  $St \approx 0.006$ . Note that, the availability of more snapshots will result in a better convergence of the peak frequency associated with streaks.

### Appendix B. Conditional averaging: sensitivity of parameter, $c$

Figures 20 and 21 show the effect of varying  $c$  in equations 3.1 and 3.2 on the obtained  $\langle \omega_x^{c1} \rangle$  and  $\langle \omega_x^{c2} \rangle$  fields, respectively, at a representative location of  $x/D = 40$ . In both figures, changing  $c$  between 0 to 1 has little qualitative effect on the distribution of negative and positive vortices around the conditioning point. It is interesting to note, however, that the  $\langle \omega_x^{c2} \rangle$  field is more robust to changes in  $c$  than the  $\langle \omega_x^{c1} \rangle$  field. Increasing the value of  $c$  leads to the capture of more intense events; but, it also reduces the number of realizations available for averaging. Hence, based on figure 7,  $c = 0.5$  is selected as a compromise between capturing intense events and having sufficient realizations for temporal averaging.

### Appendix C. Scale specific production and non-linear transfer terms in the disk wake for $m = 2$ , $St \rightarrow 0$ mode

Fourier modes and Welch estimation are employed to compute the scale-specific production and nonlinear transfer terms. The mathematical form of these two terms is as follows.

The scale-specific production term is

$$\mathcal{P}(m, St) = -\text{Re} \left[ \hat{u}_j^*(m, St) \hat{u}_i(m, St) \frac{\partial U_j}{\partial x_i} \right], \quad (\text{C } 1)$$



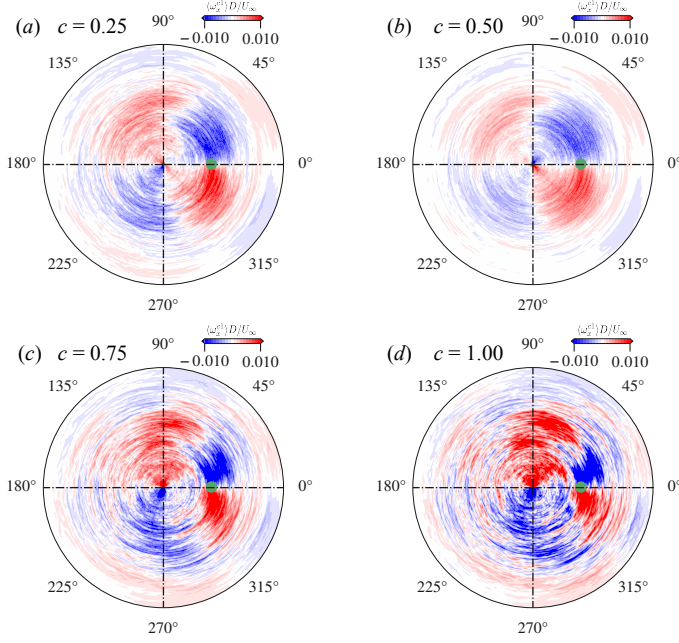


Figure 20: Effect of changing  $c$  on the conditionally averaged streamwise vorticity  $\langle \omega_x^{c1} \rangle$  obtained from  $u'_x$  based conditioning at  $x/D = 40$ .

where,  $\text{Re}[\cdot]$  denotes the real part. We are specifically interested in the production term by lateral mean shear operating on the  $m = 2, St \rightarrow 0$  mode:

$$\mathcal{P}_{xr}(m = 2, St \rightarrow 0) = -\text{Re} \left[ \hat{u}_x^* \hat{u}_r \frac{\partial U}{\partial r} \right]_{(m=2, St \rightarrow 0)}. \quad (\text{C } 2)$$

The scale-specific nonlinear transfer is

$$\mathcal{T}_{nl}(m, St) = -\text{Re} \left[ \hat{u}_j^*(m, St) \widehat{\frac{\partial u_j}{\partial x_i}}(m, St) \right] \quad (\text{C } 3)$$

This term represents the total nonlinear transfer term that generates the frequency  $St$  and wavenumber  $m$ . For identifying the triadic energy transfer, i.e.,  $m_1 + m_2 = m_3$  and  $St_1 + St_2 = St_3$ , following Cho *et al.* (2018), we write this term in discretized convolution:

$$\mathcal{T}_{nl}(m_3, St_3) = -\text{Re} \left[ \hat{u}_j^*(m_3, St_3) \sum_{\substack{St_1 + St_2 = St_3 \\ m_1 + m_2 = m_3}} \hat{u}_i(m_1, St_1) \frac{\partial \hat{u}_j}{\partial x_i}(m_2, St_2) \right] \quad (\text{C } 4)$$

For a single triad  $[m_1, m_2, m_3]$ ,  $[St_1, St_2, St_3]$  this is expanded as follows:

$$\mathcal{T}_{nl}[(m_1, m_2, m_3), (St_1, St_2, St_3)] = -\text{Re} \left[ \hat{u}_j^*(m_3, St_3) \hat{u}_i(m_1, St_1) \frac{\partial \hat{u}_j}{\partial x_i}(m_2, St_2) \right] \quad (\text{C } 5)$$

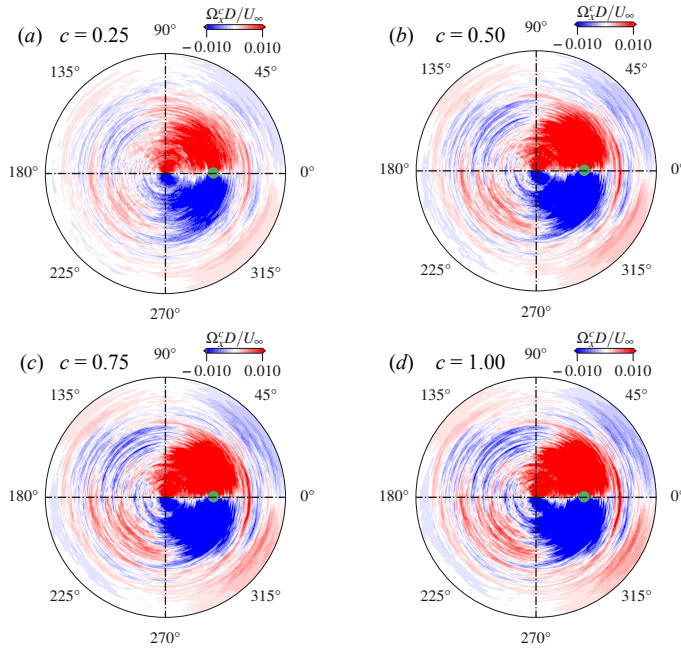


Figure 21: Effect of changing  $c$  on the conditionally averaged streamwise vorticity  $\langle \omega_x^{c^2} \rangle$  obtained from  $u'_x u'_r$  based conditioning at  $x/D = 40$ .

The nonlinear term of our interest is the one responsible for transfer of energy from the VS mode to the  $m = 2, St \rightarrow 0$  mode:

$$\mathcal{T}_{nl}[(1, 1, 2), (0.135, -0.135, 0)] = -\text{Re} \left[ \hat{u}_j^*(2, 0) \hat{u}_i(1, 0.135) \frac{\partial \hat{u}_j}{\partial x_i}(1, -0.135) \right]. \quad (\text{C } 6)$$

## REFERENCES

- ABREU, L. I., CAVALIERI, A. V. G., SCHLATTER, P., VINUESA, R. & HENNINGSON, D. S. 2020 Spectral proper orthogonal decomposition and resolvent analysis of near-wall coherent structures in turbulent pipe flows. *J. Fluid Mech.* **900**, A11.
- ANTONIA, R. A. & MI, J. 1998 Approach towards self-preservation of turbulent cylinder and screen wakes. *Exp. Therm. Fluid Sci.* **17** (4), 277–284.
- BAE, H. J., LOZANO-DURAN, A. & McKEON, B. J. 2021 Nonlinear mechanism of the self-sustaining process in the buffer and logarithmic layer of wall-bounded flows. *J. Fluid Mech.* **914**, A3.
- BALARAS, E. 2004 Modeling complex boundaries using an external force field on fixed Cartesian grids in large-eddy simulations. *Comput. Fluids* **33** (3), 375–404.
- BERGER, E., SCHOLZ, D. & SCHUMM, M. 1990 Coherent vortex structures in the wake of a sphere and a circular disk at rest and under forced vibrations. *J. Fluids Struct.* **4** (3), 231–257.
- BERNAL, L. P. & ROSHKO, A. 1986 Streamwise vortex structure in plane mixing layers. *J. Fluid Mech.* **170**, 499–525.
- BORONIN, S.A., HEALEY, J.J. & SAZHIN, S.S. 2013 Non-modal stability of round viscous jets. *J. Fluid Mech.* **716**, 96–119.
- BRANDT, L. 2007 Numerical studies of the instability and breakdown of a boundary-layer low-speed streak. *Eur. J. Mech. B/Fluids* **26** (1), 64–82.

- BRANDT, L. 2014 The lift-up effect: the linear mechanism behind transition and turbulence in shear flows. *Eur. J. Mech. B* **47**, 80–96.
- BRONEZ, T. P. 1992 On the performance advantage of multitaper spectral analysis. *IEEE Trans. Signal Process.* **40** (12), 2941–2946.
- BROWN, G. L. & ROSHKO, A. 1974 On density effects and large structure in turbulent mixing layers. *J. Fluid Mech.* **64** (4), 775–816.
- CANNON, S., CHAMPAGNE, F. & GLEZER, A. 1993 Observations of large-scale structures in wakes behind axisymmetric bodies. *Exp. Fluids* **14** (6), 447–450.
- CAVALIERI, A. V. G., REMPEL, E. L. & NOGUEIRA, P. A. S. 2022 Transition to chaos in a reduced-order model of a shear layer. *J. Fluid Mech.* **932**, A43.
- CHO, M., HWANG, Y. & CHOI, H. 2018 Scale interactions and spectral energy transfer in turbulent channel flow. *J. Fluid Mech.* **854**, 474–504.
- CHONGSIRIPINYO, K. & SARKAR, S. 2020 Decay of turbulent wakes behind a disk in homogeneous and stratified fluids. *J. Fluid Mech.* **885**, A31.
- CORINO, E. R. & BRODKEY, R. S. 1969 A visual investigation of the wall region in turbulent flow. *J. Fluid Mech.* **37** (1), 1–30.
- DAIRAY, T., OBLIGADO, M. & VASSILICOS, J. C. 2015 Non-equilibrium scaling laws in axisymmetric turbulent wakes. *J. Fluid Mech.* **781**, 166–195.
- DELVILLE, J. 1994 Characterization of the organization in shear layers via the proper orthogonal decomposition. *Appl. Sci. Res.* **53** (3), 263–281.
- ELLINGSEN, T. & PALM, E. 1975 Stability of linear flow. *Phys. Fluids* **18** (4), 487.
- FARRELL, B. F. & IOANNOU, P. J. 2012 Dynamics of streamwise rolls and streaks in turbulent wall-bounded shear flow. *J. Fluid Mech.* **708**, 149–196.
- FUCHS, H. V., MERCKER, E. & MICHEL, U. 1979a Large-scale coherent structures in the wake of axisymmetric bodies. *J. Fluid Mech.* **93** (1), 185–207.
- FUCHS, H. V., MERCKER, E. & MICHEL, U. 1979b Large-scale coherent structures in the wake of axisymmetric bodies. *J. Fluid Mech.* **93** (1), 185–207.
- GERMANO, M., PIOMELLI, U., MOIN, P. & CABOT, W. H. 1991 A dynamic subgrid-scale eddy viscosity model. *Phys. Fluids* **3** (7), 1760–1765.
- GLAUSER, M. N. & GEORGE, W. K. 1992 Application of multipoint measurements for flow characterization. *Exp. Therm. and Fluid Sci.* **5** (5), 617–632.
- GLAUSER, M. N., LEIB, S. J. & GEORGE, W. K. 1987 Coherent structures in the axisymmetric turbulent jet mixing layer. In *Turbulent Shear Flows 5*, pp. 134–145. Springer.
- GOLA, D., NIDHAN, S., ORTIZ-TARIN, J. L. & SARKAR, S. 2023 Disk wakes in nonlinear stratification. *J. Fluid Mech.* **956**, A5.
- GOPARAJU, H. & GAITONDE, D. V. 2022 Role of entropic instabilities in laminar-turbulent transition on a blunted flat plate. *Phys. Rev. Fluids* **7** (10), 103901.
- GUALTIERI, P., CASCIOLA, C. M., BENZI, R., AMATI, G. & PIVA, R. 2002 Scaling laws and intermittency in homogeneous shear flow. *Phys. Fluids* **14** (2), 583–596.
- HAMILTON, J. M., KIM, J. & WALEFFE, F. 1995 Regeneration mechanisms of near-wall turbulence structures. *J. Fluid Mech.* **287**, 317–348.
- HELLSTRÖM, L. H. O., MARUSIC, I. & SMITS, A. J. 2016 Self-similarity of the large-scale motions in turbulent pipe flow. *J. Fluid Mech.* **792**, R1.
- HUTCHINS, N. & MARUSIC, I. 2007 Evidence of very long meandering features in the logarithmic region of turbulent boundary layers. *J. Fluid Mech.* **579**, 1–28.
- JIMÉNEZ, J. 2018 Coherent structures in wall-bounded turbulence. *J. Fluid Mech.* **842**.
- JIMÉNEZ, J. & PINELLI, A. 1999 The autonomous cycle of near-wall turbulence. *J. Fluid Mech.* **389**, 335–359.
- JIMÉNEZ-GONZÁLEZ, J. I. & BRANCHER, P. 2017 Transient energy growth of optimal streaks in parallel round jets. *Phys. Fluids* **29** (11), 114101.
- JOHANSSON, P. B. V. & GEORGE, W. K. 2006 The far downstream evolution of the high-Reynolds-number axisymmetric wake behind a disk. Part 2. Slice proper orthogonal decomposition. *J. Fluid Mech.* **555**, 387.
- JOHANSSON, P. B. V., GEORGE, W. K. & WOODWARD, S. H. 2002 Proper orthogonal decomposition of an axisymmetric turbulent wake behind a disk. *Phys. Fluids* **14** (7), 2508.
- KANG, H. S. & MENEVEAU, C. 2002 Universality of large eddy simulation model parameters across a turbulent wake behind a heated cylinder. *J. Turbul.* **3** (1), 032.

- KIM, H. T., KLINE, S. J. & REYNOLDS, W. C. 1971 The production of turbulence near a smooth wall in a turbulent boundary layer. *J. Fluid Mech.* **50** (1), 133–160.
- KLINE, S. J., REYNOLDS, W. C., SCHRAUB, F. A. & RUNSTADLER, P. W. 1967 The structure of turbulent boundary layers. *J. Fluid Mech.* **30** (4), 741–773.
- LANDAHL, M. T. 1975 Wave breakdown and turbulence. *SIAM J. Appl. Math.* **28** (4), 735–756.
- LASAGNA, D., BUXTON, O. R. H. & FISCALETTI, D. 2021 Near-field coherent structures in circular and fractal orifice jets. *Phys. Rev. Fluids* **6** (4), 044612.
- LIEPMANN, D. & GHARIB, M. 1992 The role of streamwise vorticity in the near-field entrainment of round jets. *J. Fluid Mech.* **245** (-1), 643.
- LU, S. S. & WILLMARTH, W. W. 1973 Measurements of the structure of the reynolds stress in a turbulent boundary layer. *J. Fluid Mech.s* **60** (3), 481–511.
- LUMLEY, J. L. 1967 The structure of inhomogeneous turbulent flows. *Atmospheric Turbulence and Radio Wave Propagation* pp. 166–178.
- LUMLEY, J. L. 1970 *Stochastic Tools in Turbulence*. Academic Press.
- MAIA, I., JORDAN, P., HEIDT, L., COLONIUS, T., NEKKANTI, A. & SCHMIDT, O. T. 2021 Nonlinear dynamics of forced wavepackets in turbulent jets. In *AIAA Aviation 2021 Forum*, p. 2277.
- MARANT, M. & COSSU, C. 2018 Influence of optimally amplified streamwise streaks on the Kelvin–Helmholtz instability. *J. Fluid Mech.* **838**, 478–500.
- MIZUNO, Y. & JIMÉNEZ, J. 2013 Wall turbulence without walls. *J. Fluid Mech.* **723**, 429–455.
- MOCZARSKI, L., TRELEAVEN, N. C., OBERLEITHNER, K., SCHMIDT, S., FISCHER, A. & KAISER, T. L. 2022 Interaction of multiple linear helical modes in the turbulent flow field of an industrial fuel injection system. In *AIAA SciTech 2022 Forum*, p. 1061.
- MONTY, J. P., STEWART, J. A., WILLIAMS, R. C. & CHONG, M. S. 2007 Large-scale features in turbulent pipe and channel flows. *J. Fluid Mech.* **589**, 147–156.
- NEKKANTI, A., MAIA, I. A., JORDAN, P., HEIDT, L., COLONIUS, T. & SCHMIDT, O. T. 2022 Triadic nonlinear interactions and acoustics of forced versus unforced turbulent jets. In *12th International Symposium on Turbulence and Shear Flow Phenomena (TSFP12)*. Osaka, Japan.
- NEKKANTI, A. & SCHMIDT, O. T. 2021 Frequency–time analysis, low-rank reconstruction and denoising of turbulent flows using spod. *J. Fluid Mech.* **926**, A26.
- NEKKANTI, A. & SCHMIDT, O. T. 2023 Gappy spectral proper orthogonal decomposition. *J. Comput. Phys.* **478**, 111950.
- NEKKANTI, AKHIL, SCHMIDT, O. T., MAIA, I., JORDAN, P., HEIDT, L. & COLONIUS, T. 2023 Bispectral mode decomposition of axisymmetrically and non-axisymmetrically forced turbulent jets. In *AIAA AVIATION 2023 Forum*, p. 3651.
- NIDHAN, S., CHONGSIRIPINYO, K., SCHMIDT, O. T. & SARKAR, S. 2020 Spectral proper orthogonal decomposition analysis of the turbulent wake of a disk at  $Re = 50\,000$ . *Phys. Rev. Fluids* **5** (12), 124606.
- NIDHAN, S., SCHMIDT, O. T. & SARKAR, S. 2022 Analysis of coherence in turbulent stratified wakes using spectral proper orthogonal decomposition. *J. Fluid Mech.* **934**, A12.
- NOGUEIRA, P. A. S. & CAVALIERI, A. V. G. 2021 Dynamics of shear-layer coherent structures in a forced wall-bounded flow. *J. Fluid Mech.* **907**, A32.
- NOGUEIRA, P. A. S., CAVALIERI, A. V. G., JORDAN, P. & JAUNET, V. 2019 Large-scale streaky structures in turbulent jets. *J. Fluid Mech.* **873**, 211–237.
- OBLIGADO, M., DAIRAY, T. & VASSILICOS, J. C. 2016 Nonequilibrium scalings of turbulent wakes. *Phys. Rev. Fluids* **1** (4), 044409.
- ORTIZ-TARIN, J. L., NIDHAN, S. & SARKAR, S. 2021 High-Reynolds number wake of a slender body. *J. Fluid Mech.* **261**, 333–374.
- ORTIZ-TARIN, J. L., NIDHAN, S. & SARKAR, S. 2023 The high-reynolds-number stratified wake of a slender body and its comparison with a bluff-body wake. *J. Fluid Mech.* **957**, A7.
- PATEL, H. D. & YEH, C. A. 2023 Modal analysis for three-dimensional instability coupling mechanisms in turbulent wake flows over an airfoil. In *AIAA SCITECH 2023 Forum*, p. 1987.
- PICKERING, E., RIGAS, G., NOGUEIRA, P. A. S., CAVALIERI, A. V. G., SCHMIDT, O. T. & COLONIUS, T. 2020 Lift-up, Kelvin–Helmholtz and Orr mechanisms in turbulent jets. *J. Fluid Mech.* **896**, A2.
- SAMIE, M., APARECE-SCUTARIU, V., LAVOIE, P., SHIN, D. & POLLARD, A. 2022 Three-dimensional large-scale and very-large-scale coherent structures in a turbulent axisymmetric jet. *J. Fluid Mech.* **948**, A29.
- SCHMIDT, O. T. 2020 Bispectral mode decomposition of nonlinear flows. *Nonlinear Dyn.* **102** (4), 2479–2501.

- SCHMIDT, O. T. 2022 Spectral proper orthogonal decomposition using multitaper estimates. *Theor. Comput. Fluid Dyn.* **36** (5), 741–754.
- SCHMIDT, O. T. & COLONIUS, T. 2020 Guide to spectral proper orthogonal decomposition. *AIAA Journal* **58** (3), 1023–1033.
- SCHMIDT, O. T., TOWNE, A., RIGAS, G., COLONIUS, T. & BRES, G. A. 2018 Spectral analysis of jet turbulence. *J. Fluid Mech.* **855**, 953–982.
- SMITH, C. R. & METZLER, S. P. 1983 The characteristics of low-speed streaks in the near-wall region of a turbulent boundary layer. *J. Fluid Mech.* **129**, 27–54.
- TANEDA, S. 1978 Visual observations of the flow past a sphere at Reynolds numbers between  $10^4$  and  $10^6$ . *J. Fluid Mech.* **85** (1), 187–192.
- THOMSON, D. J. 1982 Spectrum estimation and harmonic analysis. *Proc. Inst. Electr. Electron. Eng.* **70** (9), 1055–1096.
- TOWNE, A., SCHMIDT, O. T. & COLONIUS, T. 2018 Spectral proper orthogonal decomposition and its relationship to dynamic mode decomposition and resolvent analysis. *J. Fluid Mech.* **847**, 821–867.
- UBEROI, M. S. & FREYMUTH, P. 1970 Turbulent energy balance and spectra of the axisymmetric wake. *Phys. Fluids* **13** (9), 2205–2210.
- WALEFFE, F. 1997 On a self-sustaining process in shear flows. *Phys. Fluids* **9** (4), 883–900.
- WALLACE, J. M. 2016 Quadrant analysis in turbulence research: history and evolution. *Annu. Rev. Fluid Mech.* **48**, 131–158.
- WELCH, P. 1967 The use of fast Fourier transform for the estimation of power spectra: a method based on time averaging over short, modified periodograms. *IEEE Transactions on Audio and Electroacoustics* **15** (2), 70–73.
- YUN, G., KIM, D. & CHOI, H. 2006 Vortical structures behind a sphere at subcritical Reynolds numbers. *Phys. Fluids* **18** (1), 015102.